Project Number: ME-JDV-0902

Switch-Mode Continuously Variable Transmission

A Major Qualifying Project Report

Submitted to the Faculty

of the

WORCESTER POLYTECHNIC INSTITUTE

in partial fulfillment of the requirements for the

Degree of Bachelor of Science

in Mechanical Engineering

by

Jeffrey M. Araujo

Michael A. DeMalia

Christopher M. Lambusta

Anthony J. Morocco

Date: April 30, 2009

Approved:

Prof. J. D. Van de Ven, Major Advisor

keywords
1. Transmission
2. Efficiency
3. Flywheel

Sponsored by: SolidWorks Corporation

Abstract

A primary challenge of a flywheel hybrid system is coupling a high speed flywheel to a vehicle's drive train. A unique way of accomplishing this task is using a switch-mode continuously variable transmission (CVT), which is the mechanical analog of a DC-DC power electronics converter. Through this project, detailed modeling and analysis was conducted of the major components of a full size passenger vehicle switch-mode CVT. This model was scaled down to allow for the design and manufacturing of a benchtop prototype. Experimental data taken from the prototype was used to verify proof of concept and quantify the nature and magnitude of system losses. The analysis concluded that the system is feasible but future research is required in the areas of design and manufacturability.

Table of Contents

Introduction 1
Background 3
CVT Research 3
Infinitely Variable Transmission 3
Variable Diameter Pulley 4
Toroidal CVT 5
Hydrostatic CVT 6
Conical CVT 6
Radial Roller CVT 7
Vibrations 8
Methodology 15
Theoretical Model 15
High Speed Clutch 20
Input Flywheel 23
Spring design 33
Prototype 36
Clutches 37
Flywheels 37
Spring Assembly Design 39
Mating the Flywheels to Respective Shafts 41
Bearings 42
Supports and Base 42
Blast Shield 42
Data Acquisition and Counting 43
Results 48
Spring Rate 48
Frictional Losses 48
Prototype Testing 50
250 RPM Trial 50
500 RPM Trial 53

900 RPM Trial 57
Discussion 61
Spring Rate 61
Frictional Losses 61
Input 62
Intermediate 63
Output 64
Conclusions and Recommendations 65
References 67
Appendices 69
Appendix A: MATLAB Code 69
Appendix B: Deflection Calculations 70
Appendix C: Clutch VI 72
Appendix D: Encoder VI 73

List of Figures

Figure 1: Diagram of the Switch Mode CVT 1
Figure 2: Range of Transmission (CVT, 2005) 4
Figure 3: V-Belt Transmission with a Various Pitch Radius (Bonsen, 2006) 5
Figure 4: Schematic of toroidal CVT (Green Car Congress, 2008) 5
Figure 5: Diagram of Hydrostatic CVT 6
Figure 6: Conical CVT 7
Figure 7: Radial Roller CVT 8
Figure 8: Comfort Levels vs. Vibration Frequency 9
Figure 9: Daily Exposure Graph 11
Figure 10: Daily Exposure Nomogram 12
Figure 11: Weighted and Linear Acceleration felt in vehicle 13
Figure 12: Initial Prototype Concept 15
Figure 13: Stored Energy in Flywheels 17
Figure 14: Clutch Engagement Profile 17
Figure 15: Angular Velocities of Shafts 18
Figure 16: Angular Position of Intermediate and Output Shaft 19
Figure 17: Torque within Spring 19
Figure 18: Clutch Engagement Profile 23
Figure 19: Personal Vehicle Miles Driven Daily 24
Figure 20: EPA Urban Dynamometer Driving Schedule 24
Figure 21: EPA UDD Force vs. Time 26
Figure 22: EPA UDD Torque vs. Time 26
Figure 23: Flywheel with Indicated Radius 28
Figure 24: Failure of Isotropic Material (Edited, Source: Widmer & von Burg, 1995) 29
Figure 25: Ashby Chart for Density and Tensile Strength of Flywheel Materials 31
Figure 26: Stress Distribution Graph Input Flywheel 32
Figure 27: Spring iteration 1 34
Figure 28: Spring iteration 3 35
Figure 29: Final spring design 35
Figure 30: Stresses of final spring design 36
Figure 31: Engagement Times of Clutch 37
Figure 32: Stresses Within the Input and Output Flywheels 38
Figure 33: Spring Cap Components 39
Figure 34: Spring CAD Model 40
Figure 35: Manufactured Spring 40
Figure 36: Deflection in Spring 41
Figure 37: Stresses in Spring 41
Figure 38: Shaft Locking Collar 42
Figure 39: Wiring Schematic (UMN, 2009) 43

Figure 40: Digikey Encoder (Digikey, 2009) 44
Figure 41: US Digital Encoder (US Digital, 2009) 44
Figure 42: Cross-sectional view of CAD model 46
Figure 43: Full CAD Model 47
Figure 44: Benchtop Prototype 47
Figure 45: Frictional Loss of Input Flywheel 49
Figure 46: Frictional Loss of Output Flywheel 49
Figure 47: Input Flywheel Position Graph 51
Figure 48: Input Flywheel Velocity Graph 51
Figure 49: Intermediate Shaft Position Graph 52
Figure 50: Intermediate Shaft Velocity Graph 52
Figure 51: Output Flywheel Position Graph 53
Figure 52: Output Flywheel Velocity Graph 53
Figure 53: Input Flywheel Position Graph - 500 rpm 54
Figure 54: Input Flywheel Velocity Graph - 500 rpm 55
Figure 55: Intermediate Shaft Position Graph - 500 rpm 55
Figure 56: Intermediate Shaft Velocity Graph - 500 rpm 56
Figure 57: Output Flywheel Position Graph - 500 rpm 56
Figure 58: Output Flywheel Velocity Graph - 500 rpm 57
Figure 59: Input Flywheel Position Graph - 900 rpm 58
Figure 60: Input Flywheel Velocity Graph - 900 rpm 58
Figure 61: Intermediate Shaft Position Graph - 900 rpm 59
Figure 62: Intermediate Shaft Velocity Graph - 900 rpm 59
Figure 63: Output Flywheel Position Graph - 900 rpm 60
Figure 64: Output Flywheel Velocity Graph - 900 rpm 60
Figure 65: Intermediate Shaft Position 63
Figure 66: Spring Failure 66

List of Tables

Table 1: Comfort Levels for Varying Vibration Magnitudes (Nakashima, 2004) 9
Table 2: Symptoms corresponding to certain frequencies 14
Table 3: Independent Variables and Initial Conditions 16
Table 4: Variables for Torque Calculation 22
Table 5: Strength to Density Ratio of Common Materials 31
Table 6: Geometric Dimensions and Speed 32
Table 7: Staggered configurations 34
Table 8: Non-staggered configurations 35
Table 9: Input and Output Flywheel Dimensions 38

Nomenclature

In alphabetical order

A_f - Frontal area of the vehicle

A(t) - Instantaneous acceleration

C_d - Drag coefficient

C_{rr} - Coefficient of rolling resistance

CVT - Continuously Variable Transmission

DAQ - Data Acquisition

DoT - Department of Transportation

E_f - Energy storage of flywheel

E_v - Energy required to apply torque for a set angular position

EPA - Environmental Protection Agency

$F_d(t)$ - Drag force

F_{dmax} - Maximum drag force

F_i - Inertial force

F_{rr} - Force to overcome rolling resistance

$F_v(t)$ - Vehicle force

F_{vmax} - Maximum vehicle force

I_f - Mass moment of inertia

ISO - International Organization for Standards

IVT - Infinitely Variable Transmission

M_v - Mass of passenger vehicle

NI - National Instruments

PAR - Peak to Average Ratio

T_0 - Time step n-1

T_1 - Time step n

T_v - Applied vehicle torque

UDDS - Urban Dynamometer Driving Schedule

V(t) - Velocity at time step n

V(t-1) - Velocity at time step n-1

a_v - Acceleration of vehicle

g – Gravitational constant

r - Radius of interest

r_f - Radius of flywheel

r_i - Inner radius

r_0 - Outer radius

r_v - Radius of tire

t - Thickness of flywheel

t_0 – Time

v - velocity of vehicle

θ - Angular position

ρ - Density of air,

ρ_f - Density of flywheel material

σ_T - Tangential stress

σ_r - Radial stress

ν_f - Poisons ratio

ω_0 - Initial angular velocity

ω_f - Angular velocity

ω_{input} - Angular velocity of input flywheel

ω_{output} - Angular velocity of output flywheel

Introduction

In the current automotive industry, there is a strong emphasis being placed on the fuel efficiency of a vehicle. This demand for efficiency is driven primarily by fluctuating fuel costs and a desire to reduce emissions. In response to this demand, hybrid vehicle sales have increased. These vehicles have proven to be efficient because they draw their power from an internal combustion engine coupled with an auxiliary power source capable of energy recovery. Although electric hybrid power trains and similar systems have proven to be more efficient than conventional vehicles, the overall efficiency of the system could be greatly improved by using an auxiliary power source, such as a flywheel, with a much higher energy and power density. However, the major problem with flywheel hybrids is coupling the high speed flywheel to the drive train of the vehicle. A novel solution to this problem, which serves as the focus of this project, is the switch mode continuously variable transmission (CVT). This transmission, a schematic of which is seen in Figure 1, uses a flywheel, clutch, anti-reverse ratchet, and spring to transmit torque from the input shaft to the output shaft (Forbes & Van de Ven, 2008). In order to understand how torque is transmitted through the system, it is necessary to describe the function of each component in the assembly and their interaction with one another.

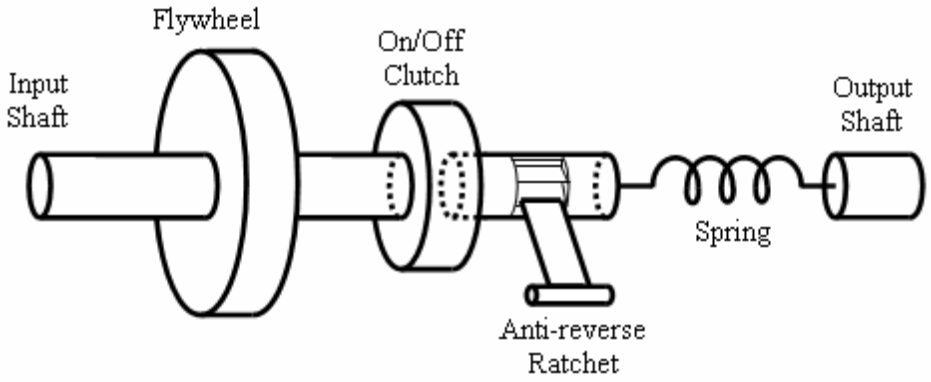

Figure 1: Diagram of the Switch Mode CVT

.

Torque enters the system from the engine, driving the input flywheel up to a desired speed of about 50,000 rpm. The energy stored in the flywheel is sent to the drive train via a clutch which pulses at a high rate of speed. When the clutch is engaged, the intermediate shaft rotates at the same speed as the clutch, creating angular deflection in the spring. The deflection

of the spring creates the desired torque at the output shaft. When the clutch is disengaged, the spring continues to apply torque to the output shaft due to the anti-reversing ratchet preventing the intermediate shaft from counter-rotating. The duty ratio, defined as the percent of the switching cycle that the clutch is engaged divide by the cycle time, determines the magnitude of the spring deflection, and thus the output torque. The varied spring deflection therefore allows the system to be thought of as an infinitely variable transmission. This infinite number of gear ratios means that at any given speed, the motor can run at its optimal range, which further increases the efficiency of the system.

This transmission also has the capability to run in a regenerative mode due to the use of a sprag clutch and a brake on the intermediate shaft. Regeneration occurs when the brake is engaged, which in turn makes the spring deflect in the opposite direction from the generative mode because the output shaft is still spinning. Once the spring absorbs the energy from the output shaft, the brake is released, causing the sprag clutch between the intermediate shaft and the flywheel to engage; once again allowing the intermediate shaft to spin and transfer energy back to the input flywheel and increase its angular velocity.

This goal of this project is to further develop the switch-mode CVT in the following ways:

- Research and develop the system requirements and performance specifications for application of this drive train in a full sized passenger vehicle.
- Design and perform analysis on a scaled prototype system that demonstrates the drive train in both generative and regenerative modes.
- Build and demonstrate a bench top prototype of the system.

Background

The background section of this report consists of information that was researched to obtain an understanding of previously conducted work and to formulate some basic design parameters. The first portion of this section consists of descriptions of other CVTs previously created and utilized in the automotive industry. This research was conducted in an effort to obtain an understanding of currently available technologies and to compare those with the switch-mode CVT proposed in this project. The second portion of the background consists of vibrational research from the ISO standards and comfort level research from Nakashima. This research will be used to assign a frequency at which pulsing the clutch will not adversely affect the passengers, and to also assign a vibrational constant that will not harm potential passengers in a full sized model.

CVT Research

A CVT is a transmission which provides a step-less transition from the lowest gears to the highest gears of the vehicle (Bonsen, 2006). CVT's are theoretically a more suitable and capable transmission than fixed gear units currently dominating the automobile market, however their acceptance by the general public has been somewhat limited until recent times (Green Car Congress, 2008). The global economy is now placing pressure on the automotive industry to create what has become known as 'green' vehicles, vehicles that consume less fossil fuel and have minimal emissions (Green Car Congress, 2008). This pressure is helping pave the way for the CVT because of the device's capability to allow engines to operate at their ideal efficiency regardless of the vehicle velocity. The idea of a step-less transmission has been around since the late 15th century when Leonardo Da Vinci first conceptualized such a device (How Stuff Works, 2008). Since then, many variations have been created. An outline of the most common CVT types along with a summary of their advantages and shortcomings is detailed below.

Infinitely Variable Transmission

An infinitely variable transmission (IVT) is a special form of CVT that provides a full range of gear ratios, including negative values, for reversing the vehicle. Figure 2 is a schematic showing the differences in the ranges between a manual transmission, a conventional CVT and an IVT.

The IVT has many advantages, including minimal torque limitations, and has very high overdrive values (Green Car Congress, 2008).

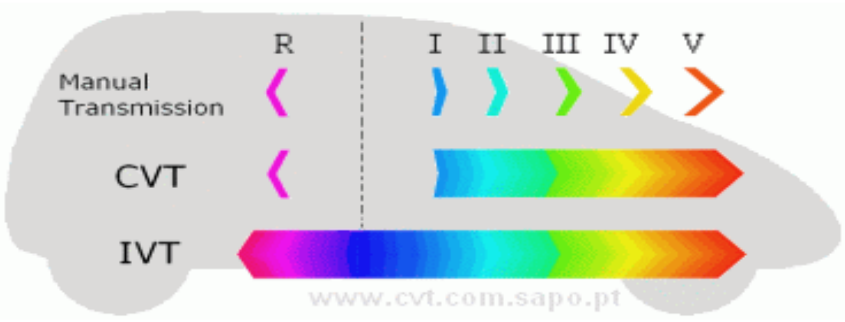

Figure 2: Range of Transmission (CVT, 2005)

Variable Diameter Pulley

The Variable Diameter Pulley CVT, commonly referred to as the Reeves CVT, is currently the most common continuously variable transmission in use. The system, seen in Figure 3, usually consists of two variable radius sheaves with a Vee-belt connecting the sheaves. When the two cones of the sheave are farther apart, the belt rides lower into the groove and what is known as the pitch radius is decreased. Consequently, when the two sheaves are closer together the belt will ride higher in the groove and there is an increase in the pitch radius. The pitch radius is equal to the effective radius of the belt at the driving end of the transmission. When the two plates of the drive pulley are pushed together closely the vehicle is in its highest "gear" and when they are pulled apart to opposite extremes the vehicle is in its "lowest" gear. The effective gear of the transmission is equal to the pitch radius divided by the radius of the opposite (driving) end of the belt (How Stuff Works, 2008). The main disadvantage with this type of CVT is its limited torque capacity. Additional disadvantages come from the frictional force present between the plates and the belt which serves to reduce overall efficiency and lower life expectancy (Bonsen, 2006).

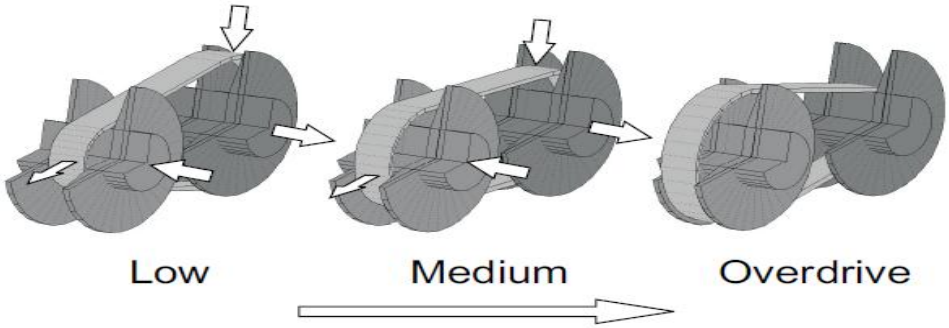

Figure 3: V-Belt Transmission with a Various Pitch Radius (Bonsen, 2006)

Toroidal CVT

A toroidal CVT is similar to the variable diameter pulley CVT, with the primary difference being that the belt is replaced by conical surfaces. In this configuration, seen in Figure 4, one of the plates is driven by the engine and the other is connected to the driveshaft of the vehicle. The conical surfaces change the angle of the axis of rotation on the conically shaped plate and determine the effective gear ratio of the vehicle, much like how the belts of the Variable Diameter Pulley CVT create an effective gear ratio. If the rollers are at the outer edge of the driven plate the vehicle is in its "lowest" gear; if the rollers are at the inner radius of the driven plate than the vehicle is in its "highest" gear (How Stuff Works, 2008).

Manufacturing is the main disadvantage of toroidal transmissions. The toroidal CVT uses minimal contact points, and therefore precision manufacturing is important. The transmission is relatively heavy compared to other transmissions due to the amount of mechanical components. Additionally, some companies choose to cool the transmission with coolant and heat exchangers, which further increases the weight (SAE, 2009).

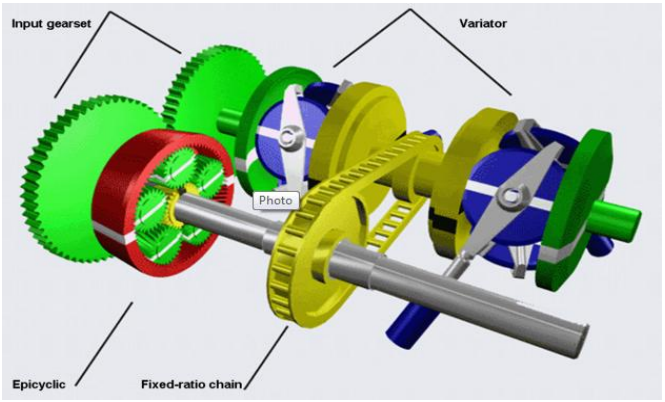

Figure 4: Schematic of toroidal CVT (Green Car Congress, 2008)

Hydrostatic CVT

The hydrostatic CVT, seen in Figure 5, is a form of infinitely variable transmission which uses variable displacement pumps to fluctuate fluid flow into hydrostatic pumps and motors. The rotational motion of the engine drives a hydraulic pump and converts the rotational energy into fluid flow. A hydraulic motor located on the output shaft converts this fluid flow back into rotational motion that can be transferred to the wheels.

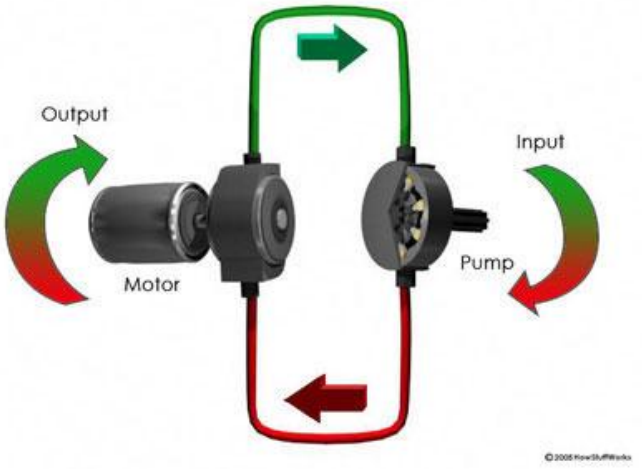

Figure 5: Diagram of Hydrostatic CVT

On many occasions, these CVTs also use gear-sets and clutches to create a hybrid system called a hydro-mechanical transmission. In this configuration, power from the engine is transferred using hydraulics at low speeds but operating mechanically at high speeds. At any point between these limits, the transmission uses various amounts of both hydraulic and mechanical power (Yoshihiro Yoshida et al, 2005). One major advantage of this system is that the hydraulic motor can be mounted directly to the driving wheel hub of the vehicle. Another advantage is the ability to eliminate frictional losses between the drive shaft and differential of the vehicle. However, there are certain tradeoffs with the system; it is expensive, the hydraulic fluid can become contaminated, and it generates a high amount of heat during high torque applications

Conical CVT

The Conical CVT operates via the motion from the engine, and that power is transmitted to the main gear, called the sun gear, seen in Figure 6. From the sun gear, the motion is

transmitted to a specified number of gears, called satellites that are attached around the sun gear. Each satellite is connected by a shaft known as a reaction ring gear and two joints to a cone-shaped body. The satellite cones transmit motion to a central hub by friction caused from the sun gear and outer ring gear. Contact between the satellite cones and the hub is maintained by a pneumatic system which pushes all the satellite cones against the hub and the outside ring. The power produced by the engine is transmitted to the output shaft by internal gears (Rondinelli, 2006).

There are some disadvantages to the conical CVT. First, the CVT is not easy to manufacture due to the precision of parts, which increases cost. Second, the transmission is a bit heavier than conventional CVTs due to the components in the conical CVT coupled with cooling components.

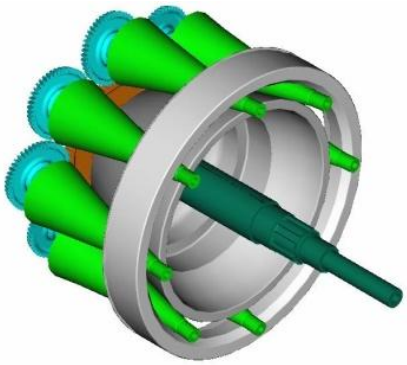

Figure 6: Conical CVT

Radial Roller CVT

A radial roller CVT, seen in Figure 7, uses two coaxial rotors (sleeves) to transfer power. Rollers are placed between the rotors and depending on the forces applied to the two different rotors, the gear ratio varies continuously. A pneumatic piston is attached to the rotor and retracts if the engine has high amounts of force overloading it, and thus the torque fed to the output decreases (note that although the torque produced may overwhelm the system, the transmission doesn't effectively stop the engine). The main problem with these CVTs is the narrow variation in transmission ratio. This problem is overcome by arranging freewheels side by side and coupling them in pairs with a common rotor. This allows a theoretically infinite transmission ratio from a very compact CVT. The advantages of this CVT are that it is inexpensive to manufacture and it has high power efficiency (Girotto, 2006).

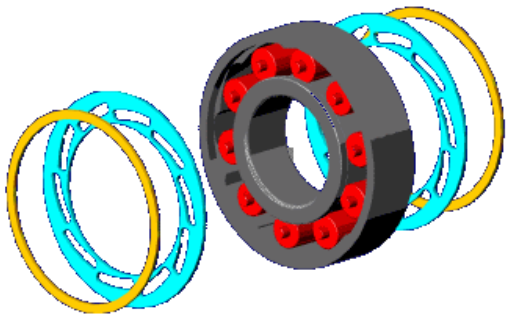

Figure 7: Radial Roller CVT

From the above conducted research on currently available CVT's, it is clear that the switch mode CVT proposed in this project is unique. This originality makes it necessary to research common mechanical and physical properties which are considered when designing a transmission. The following sections of the background are intended to provide the basis for design work that will follow in a latter part of the project. The topics addressed in the following sections include magnitude of vibrations and noise levels. These sections investigate the applicability of this device to a real world scenario by taking into consideration the overall safety of the device and its effect on human passengers.

Vibrations

The switch mode CVT relies on the operation of a clutch to supply power to the output shaft of a vehicle. The clutch operates by rapidly turning on and off and creates pulses from this switching action. This pulsing action of the clutch produces a torque ripple, which creates vibrations in the system. The frequency at which the clutch pulses therefore has an effect on the overall system vibration. A higher frequency decreases the magnitude of the vibrations, and likewise a lower frequency will increase the magnitude of the vibrations. The downside to high frequency operation is that the clutch makes a larger number of engagements, resulting in more energy loss due to frictional slip between the components. The methodology and results sections of the paper will address the energy loss due to slip between these components. However, before the frequency of the clutch can be determined, it is first necessary to research the response of humans to various vibration levels. This is important when determining the frequency because the clutch must be pulsed at such a rate that it does not produce vibrations which are felt as uncomfortable or even dangerous to the passenger.

In order to calculate the frequency at which to pulse the clutch, research was conducted in regards to human response to vibrations. The most commonly used reference to find accetable limits of vibrations on the human body is the International Organization for Standards (ISO) 2631 standard. This ISO standard sets guidelines for how to take measurements and calculate exposure statistics. Measurements of power spectral densities of tri-axial acceleration are taken in order to calculate the ISO 2631 whole-body vibration statistics. These measurements are usually taken at the seat cushion. ISO 2631 also recommends acceptable duration levels. Table 1 shows the guidelines for levels of comfort at different vibration magnitudes.

Table 1: Comfort Levels for Varying Vibration Magnitudes (Nakashima, 2004)

Vibration Level	Comfort Level
Less than 0.315 m\s^2	Not Uncomfortable
0.315 m\s^2 – 0.63 m\s^2	A little uncomfortable
0.5 m\s^2 – 1 m\s^2	Fairly Uncomfortable
0.8 m\s^2 – 1.6 m\s^2	Uncomfortable
1.25 m\s^2 – 2.5 m\s^2	Very Uncomfortable
Greater than 2 m\s^2	Extremely Uncomfortable

A study done at the University of Vermont observed the comfort levels of 10 seated people when subjected to vibrations of varying shapes and frequencies. The five shock frequencies tested were 2, 4, 5, 6, and 8 Hz. Each person rated their comfort levels on a scale from 1 to 10 when exposed to each of the vibrations, 1 representing comfortable and 10 representing very uncomfortable pain (Huston et al., 2000). The results of these experiments are shown in the Figure 8.

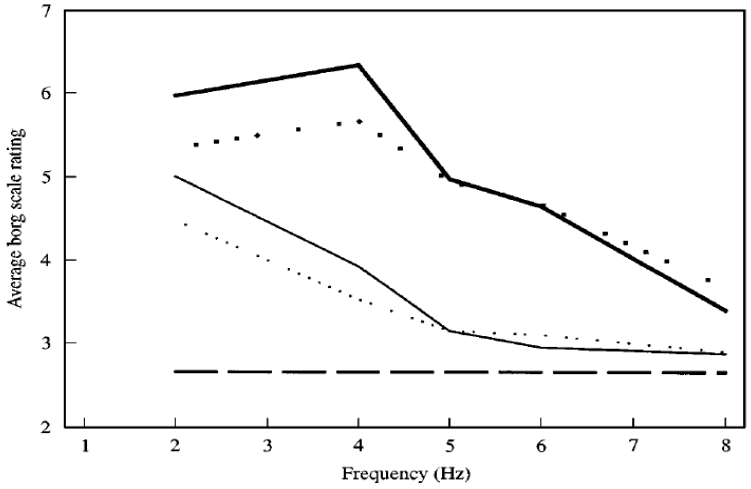

Figure 8: Comfort Levels vs. Vibration Frequency

- The upper four plots show the ratings for the shocks at 2, 4, 5, 6, and 8 Hz. The lower dashed line shows the rating for the white noise and is not frequency specific.
- The thick solid line represents a high PAR (peak to average ratio) sine-wave.
- The squares represent a high PAR half sine-wave.
- The thin solid line represents a low PAR sine-wave.
- The dotted line represents a low PAR half sine-wave.

Vibrational Exposure Graphs

In addition to the magnitude of the vibrations, exposure rates were also examined to make sure they do not become harmful to the passengers in the vehicle. Figure 9 shows the daily exposure limits that a person can handle (Griffin et. al., 2008).

The graph gives a simple alternative for looking up daily exposures or partial vibration exposures. The lower shaded area indicates exposures likely to be below the exposure action value. These exposures can be assumed "safe" for an average, healthy person (Griffin et. al., 2008). It would be ideal to stay in the lower shaded area at all costs as higher values may pose health problems for the passengers. The shaded region in the middle corresponds to accelerations and durations that my pose possible health risks while the upper region should be avoided because the vibrations and durations are hazardous to human health.

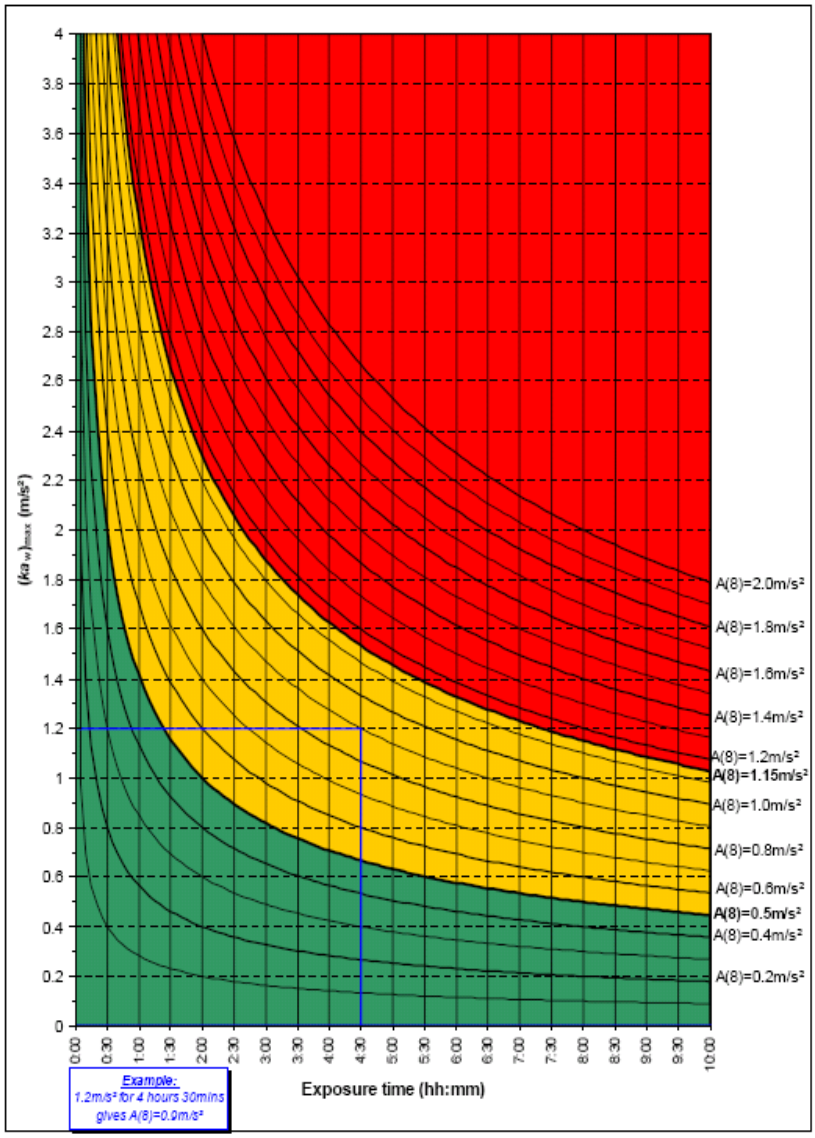

Figure 9: Daily Exposure Graph

The nomogram in Figure 10 provides another alternative of obtaining daily vibration exposures, without using the equations. On the left hand line, find the point corresponding to the vibration magnitude, use the left scale for x- and y-axis values; the right scale for z-axis values. Then, draw a line from the point on the left hand line, representing the vibration magnitude, to a point on the right hand line (representing the exposure time) and read off the partial exposures where the line crosses the central scale (Griffin et. al., 2008).

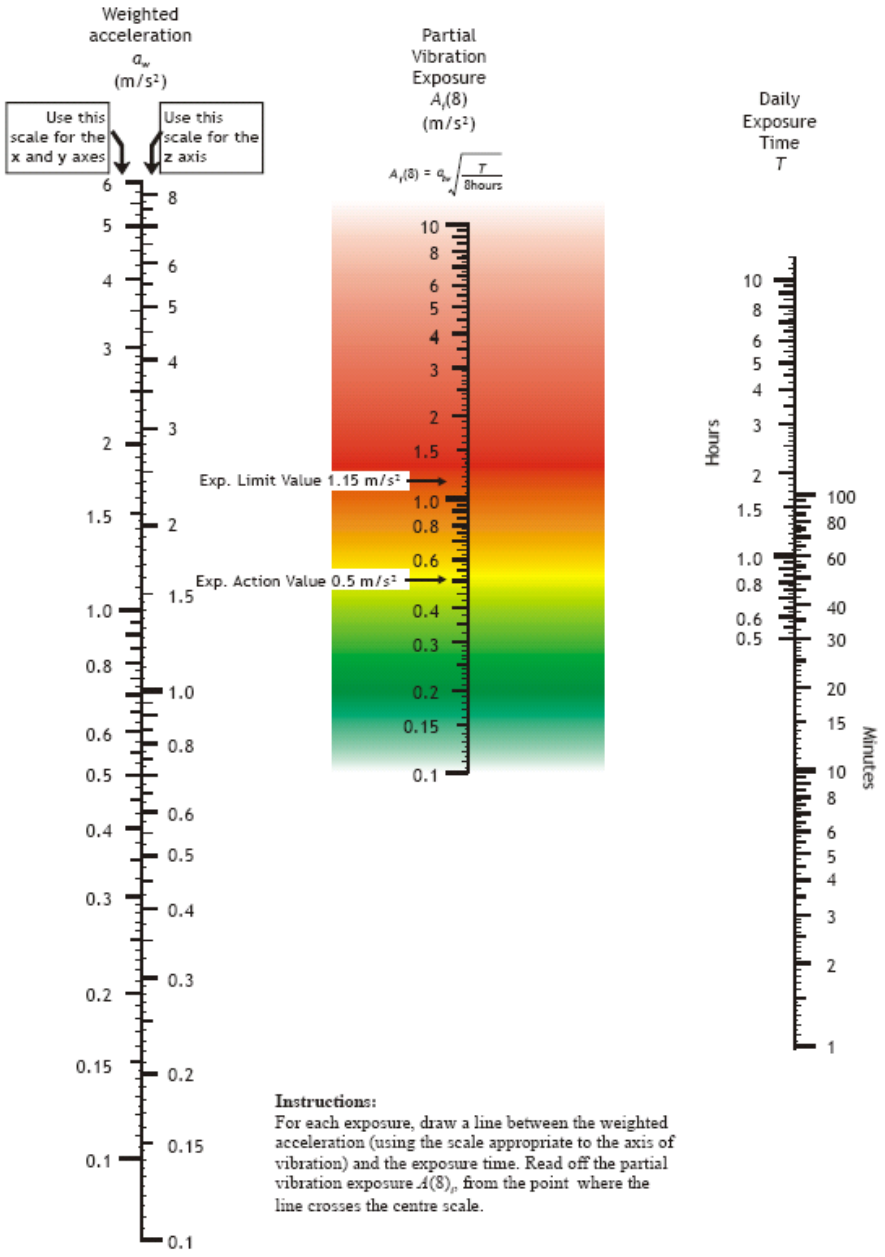

Figure 10: Daily Exposure Nomogram

Clutch Frequency Calculation

Using the study presented in Table 1, the selected threshold for maximum acceleration felt by the passengers of a vehicle was found to be 0.63 m/s^2. This value was then divided by a series of weighting factors contained within the ISO 2631 standard. Each weighting factor contains a corresponding frequency. A graph of the weighted acceleration and frequency can be seen in Figure 11. The linear acceleration profile, also seen graphically in Figure 11, was created by experimentally altering the pulsing frequency from 5 to 30 Hertz and measuring the

corresponding change in spring torque for three different pulses within a MATLAB simulation, which is explained later. The torque value obtained for each of these pulses was then averaged, and using a similar method as described above, the acceleration corresponding to this torque value was determined. The acceleration was then plotted with respect to the frequency. Ideally, the frequency at which these lines cross is the desired frequency at which to pulse the clutch.

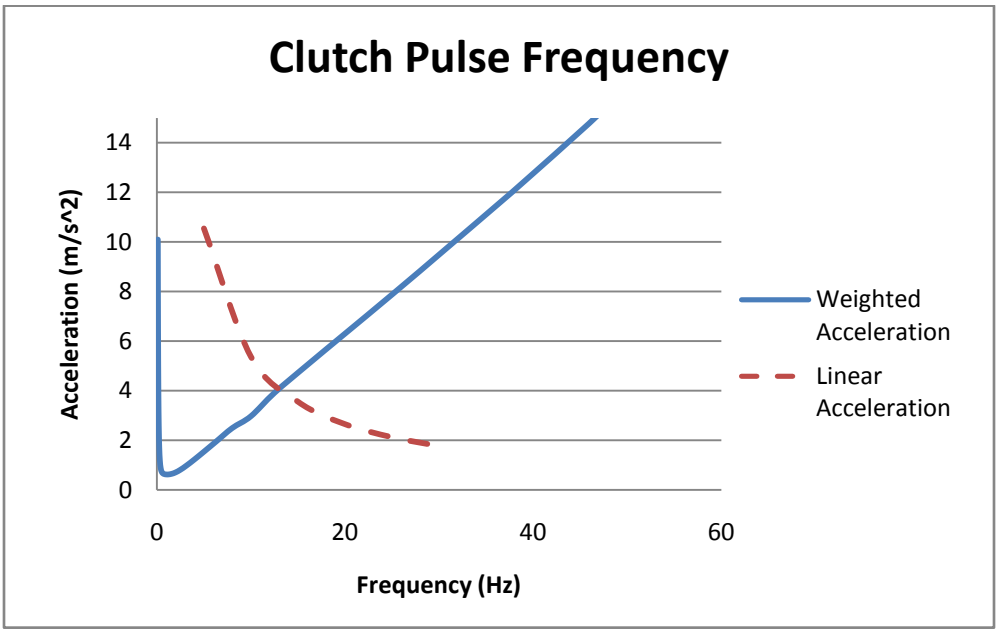

Figure 11: Weighted and Linear Acceleration felt in vehicle

Based on the data from Figure 11, it would appear as though the clutch should pulse at approximately 13 Hertz. However, studies indicate that certain frequencies below the level of 20 hertz can produce adverse side effects (Rasmussen, 2008). A listing of the frequency ranges and corresponding health risks is found in Table 2. In order to avoid complications caused by these low level frequencies, it was decided that for this project the pulsing frequency should be set at 20 Hertz.

Table 2: Symptoms corresponding to certain frequencies

Symptoms	Frequency
General feeling of discomfort	4-9
Head symptoms	13-20
Lower jaw symptoms	6-8
Influence on speech	13-20
"Lump in the throat"	12-16
Chest pains	5-7
Abdominal pains	4-10
Urge to urinate	10-18
Increased muscle tone	13-20
Influence on breathing movements	4-8
Muscle contractions	4-9

Methodology

This section was separated into two subsections: theoretical model and prototyping. The theoretical model starts with an explanation of the system as a whole, and then is broken down into components. The summary of each component discusses the interaction between other components and its functionality. The prototype section details the analysis, design, and manufacturing work completed during the project.

Theoretical Model

In order to accomplish the goals of this project, a mathematical model simulating the operation of the switch mode CVT was examined. The model of the system seen in Figure 12, was created by Tyler Forbes and James Van de Ven, and a copy of the code is contained within Appendix A. To simplify the analysis in the model, the vehicle mass is represented by a flywheel connected to the output shaft. The equations in the model calculate the energy storage and speed of the flywheels, along with the corresponding positions, velocities, and accelerations of the shafts, and also the state of the clutch. The model uses a finite-difference method across a number of incremental time steps. The operating parameters and initial conditions of the model can be found in Table 3. is a summary of the dependent variables and their initial conditions. It should be noted that any variable with a subscript of 1 refers to the input flywheel, a 2 for the intermediate shaft, and a 3 for the output flywheel.

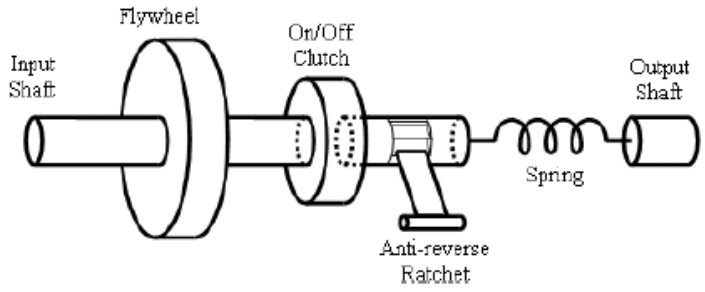

Figure 12: Initial Prototype Concept

Table 3: Independent Variables and Initial Conditions

Variable	Definition	Value
delta_t	Time step of model	0.00001 seconds
run_time	Model run time	2.5 seconds
freq	Pulse frequency	20 Hertz
duty_ratio	Fraction that clutch is on	0.009
I1	Moment of inertia of input flywheel	.328 $kg*m^2$
I3	Moment of inertia of output flywheel	211 $kg*m^2$
k	Torsional spring rate	497 N*m/rad
b	Torsional damping coefficient	0.5 $kg*m^2/s$
omega1_init	Initial angular velocity of input flywheel	2100 rad/s
omega3_init	Initial angular velocity of output flywheel	0.1 rad/s
A	Frontal area of vehicle	2.16 m^2
Cd	Aero drag coefficient	0.26
rho	Air density	1.2 kg/m^3
m	Vehicle mass	1500 kg
fo	Basic rolling resistance coefficient	0.009
fs	Speed rolling resistance coefficient	0.0035
g	Gravity	9.8 m/s^2
dia	Wheel diameter	0.75 m
theta1 (1)	Input position at first time step	0
theta2 (1)	Intermediate position at first time step	0
theta3 (1)	Output position at first time step	0
E1 (1)	Input flywheel energy at first time step	.5 * I1 * omega1 $(1)^2$
E3 (1)	Output flywheel energy at first time step	.5 * I3 * omega3 $(1)^2$
Es (1)	Spring torque at first time step	.5 * k * (theta2 (1) - theta3 $(1))^2$

After running the simulation, a series of plots were created to show the ideal operation of the transmission. Figure 13 plots the stored energy within both flywheels with respect to time. It can be seen that the input flywheel begins with approximately 720 kilojoules of energy and ends with 550 kilojoules. Therefore, 170 kilojoules transferred to the system and approximately 140 kilojoules are stored in the output flywheel. The 30 kilojoules that are lost during the simulation can be attributed to frictional losses in the system.

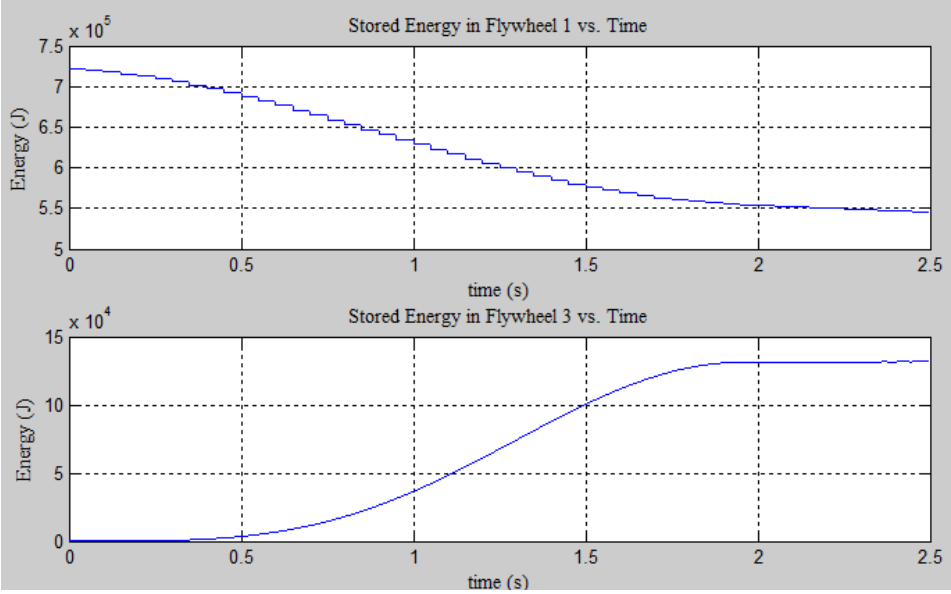

Figure 13: Stored Energy in Flywheels

Having plotted the energy, the clutch can be examined to determine how it affects the system. From Figure 13, the decreasing steps in the plot of the input flywheel are due to the engagement of the clutch and the transferring of energy into the drive train. Figure 14 plots a time interval showing two engagements of the clutch. The simulation represents an ideal case, which allows the clutch to have instantaneous engagement and disengagement. Therefore, coupled with the large input speed, the duty ratio of the system must remain small.

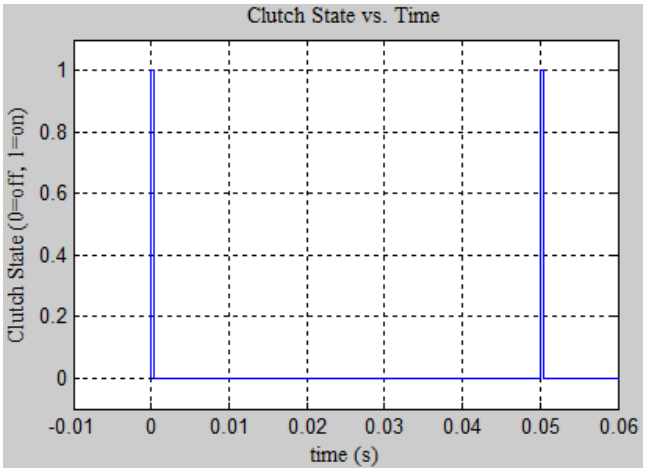

Figure 14: Clutch Engagement Profile

Figure 15 plots the angular velocity of each shaft: the input, intermediate and output, respectively. Both the input and output shaft plots have the same general trend as the energy

storage plots, which show the input speed reduction due to the clutch and a smooth speed increase in the vehicle. As for the intermediate shaft, it only rotates when the clutch is engaged and will instantaneously reach the speed of the input flywheel. Each spike in the graph corresponds to a clutch engagement, and the peak is the current speed of the input flywheel.

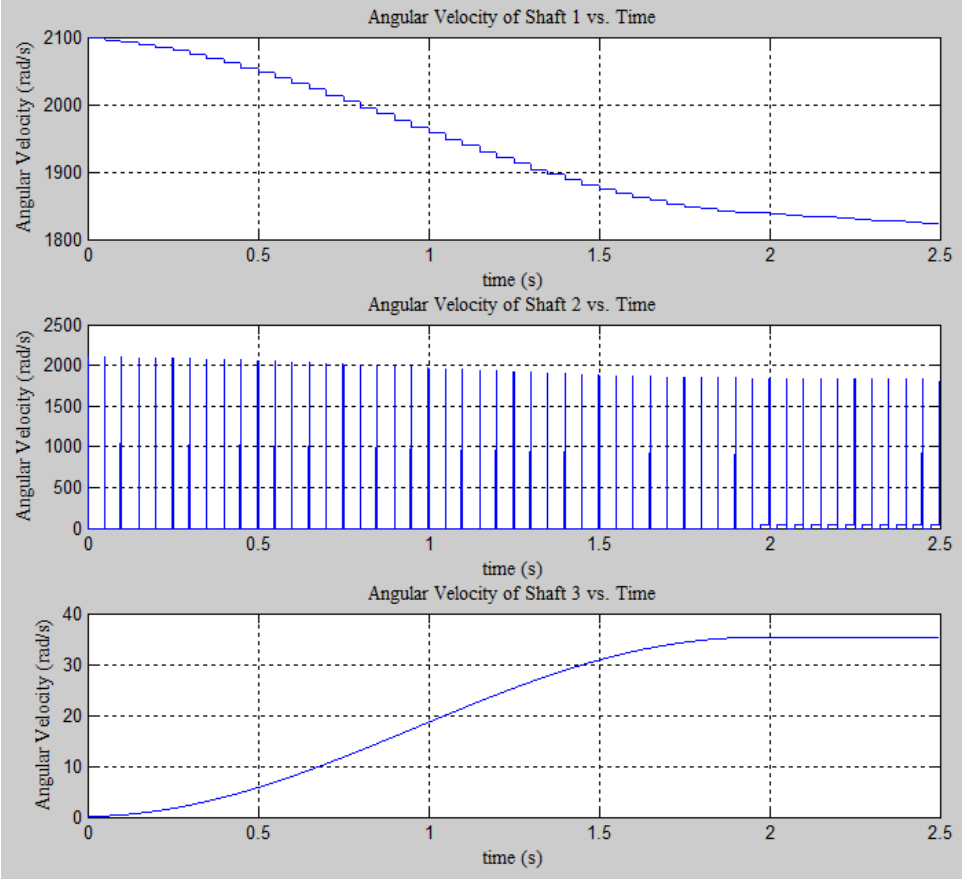

Figure 15: Angular Velocities of Shafts

Another point of interest in the model is the position of the intermediate and output shafts. Figure 16 shows the position of both shafts graphed together. As discussed, each step in the position of the intermediate shaft is due to the engagement of the clutch, while the output shaft has an exponential growth. The point at which the two lines intersect, the intermediate shaft begins to freewheel and the spring stops transmitting torque until the next clutch pulse.

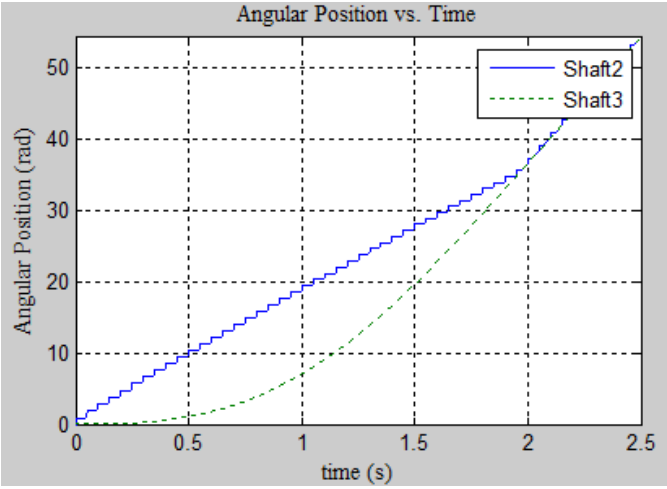

Figure 16: Angular Position of Intermediate and Output Shaft

The last plot, Figure 17, deals with the spring torque being generated in the system. This figure shows each clutch engagement with an equivalent corresponding jump in torque. At early time steps, after the torque jump has been made, the release of torque to the output flywheel is fairly small as it takes some time to accelerate a large body. However, the drop in torque around one second is approximately the same as the increase in the torque, which creates the large velocity increase in the earlier plots. Finally, the pulses which occur around two seconds are the torque to maintain the maximum speed of the output flywheel.

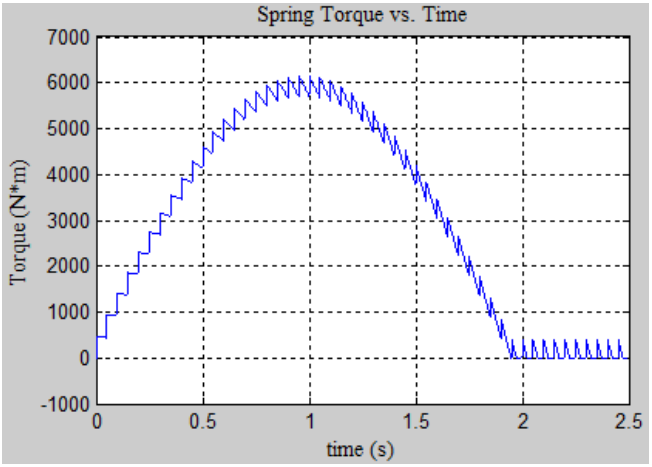

Figure 17: Torque within Spring

In reference to the Background section, a graph was created that plotted both the weighted and linear acceleration of the vehicle. The linear acceleration line was calculated by using the data from Figure 17. For each frequency, a torque step, measured as a height of a particular vertical line, was calculated. An example of this can be seen from the initial pulse on

the plot. Originally, there is no torque in the spring, then once the clutch engages, there is a torque increase of approximately 500 N*m. Several of these jumps were approximated and averaged to get a mean torque value for that particular frequency. This value was then used to create the figure seen within the Background section.

The mathematical simulation described above shows the general functionality of the system, and the constraints present on each of the major components. However, it does not give details about the size of each of these components, or their applicabilty within a passenger vehicle. The following sections provide detailed analysis and design specifications for the high speed clutch, input flywheel, and spring.

High Speed Clutch

The clutch for the switch-mode CVT needs to transfer torque at rapid time intervals to induce spring deflection. The period of time that the clutch is on is dependent on the desired deflection of the spring. When the desired deflection is achieved, the clutch will disengage. Therefore, in order to approximate the engagement profile of the clutch, the maximum torque transfer per pulse needs to be determined.

Calculating Magnitude of Torque

The maximum torque that needs to be transferred to a vehicle comes during rapid acceleration events. Typical hybrid vehicles have become synonymous with having relatively low zero to sixty times. For that reason, it was desired that the simulated vehicle should be capable of achieving this zero to sixty in approximately eight seconds. Calculating the torque necessary to produce this acceleration for the model vehicle was done in the following way:

1). Define a constant acceleration as the derivative of velocity.

$$a_v = \dot{v} = \frac{dv}{dt} \quad \textbf{(1)}$$

where a_v is the constant acceleration of the vehicle and v is the velocity of the vehicle.

2). Define all forces acting on the vehicle.

a). Calculate the Inertial Force

$$F_i = M_v * a_v \quad \textbf{(2)}$$

where F_i is the inertial force and M_v is the approximate mass of a passenger vehicle.

b). Calculate the force to overcome rolling resistance

$$F_{rr} = C_{rr} * M_v * g \quad \textbf{(3)}$$

where F_{rr} is the force to overcome rolling resistance, C_{rr} is the coefficient of rolling resistance and g is the gravitational constant.

c). Calculate Drag Force

$$F_d(t) = \frac{1}{2} * \rho * V(t)^2 * A_f * C_d \quad \textbf{(4)}$$

where $F_d(t)$ is the drag force, ρ is the density of air, A_f is the frontal area of the vehicle, and C_d is the drag coefficient.

d). Calculate total vehicle force as a function of time

$$F_v(t) = F_i + F_{rr} + F_d(t) \quad \textbf{(5)}$$

where $F_v(t)$ is the vehicle force. It should be noted that grade forces from the road are neglected. Maximum vehicle force is found when velocity is at its highest value.

e). Calculate maximum vehicle force

$$F_{vmax} = F_i + F_{rr} + F_{dmax} \quad \textbf{(6)}$$

4). Use the approximate radius of a tire to calculate maximum torque

$$T_v = F_{vmax} * r_v \quad \textbf{(7)}$$

Using this procedure and the variables shown in Table 4, it was determined that 1000 foot-pounds of torque needed to be applied to the spring to produce maximum deflection. This torque value produces an acceleration of zero to sixty in eight seconds. This value for torque does not take into account any losses aside from those of drag and rolling resistance.

Table 4: Variables for Torque Calculation

Variable	Value
A	3.126 m/s^2
M_v	1500 kg
C_{rr}	.008
G	9.807 m/s^2
ρ	1.2 kg/m^3
A_f	3 m^2
C_d	0.4
V(t)	0 – 26.82 m/s
F_{dmax}	518 N
r_v	0.254 m

Approximating Engagement Profile

The engagement profile of the clutch is based on two torques seen within the system: torque to accelerate the intermediate shaft, or the time for the clutch to fully engage, and torque generated in the spring. Due to the complexity of clutch engagement for various types of clutches, a simplified model was used where the clutch is either fully on or fully off. Therefore, there is no clutch engagement period or time necessary to accelerate the intermediate shaft up to the input flywheel speed. The only torque present in the system is the spring torque which is due to the deflection generated by the time the clutch is on. This profile, seen in Figure 18, was created by entering in the desired parameters into the MATLAB model. The plot shows the linear increase in torque up to the maximum of 1000 ft-lb.

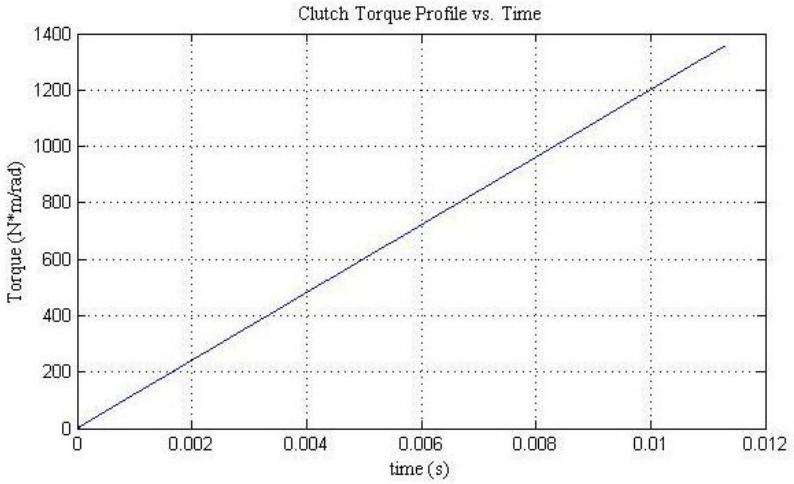

Figure 18: Clutch Engagement Profile

Input Flywheel

The input flywheel in this transmission serves to minimize the reliance of a vehicle on its combustion engine, while at the same time capturing regenerative energy that is typically lost during normal operation. For that reason, the major governing factor in its design was energy storage capabilities. Ideally, enough energy can be stored in the flywheel so that the vehicle can be driven during the course of the day without reliance on the engine. This goal can be accomplished by pre-charging the flywheel with a specified amount of energy at home with an electric motor for example, and then energy can be added during vehicle operation by capturing what is usually lost to friction during braking.

In order to quantify the required flywheel energy storage, the first step was to obtain the average daily number of miles driven by Americans. Figure 19, from the US Department of Transportation, estimates that approximately 50 percent of Americans drive 25 miles a day or less (DoT, 1998). In addition to knowing the average daily number of miles driven, the Environmental Protection Agency (EPA) Urban Dynamometer Driving Schedule (UDDS) was used to approximate the changes in velocity and acceleration that take place during normal vehicle operation. Figure 19 is a graphical representation of the data obtained. The total distance traveled in this cycle is approximately 7.45 miles.

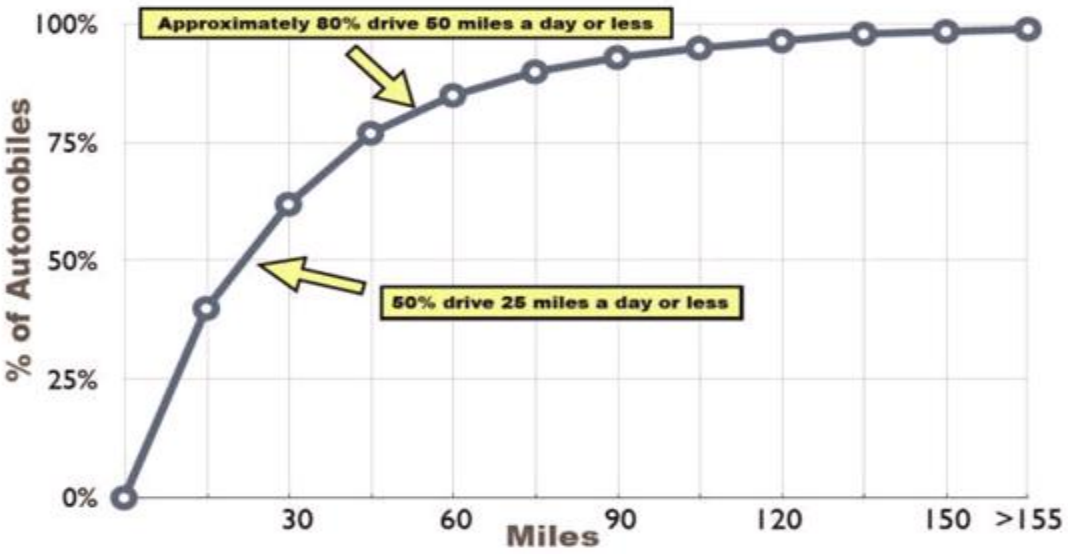

Figure 19: Personal Vehicle Miles Driven Daily

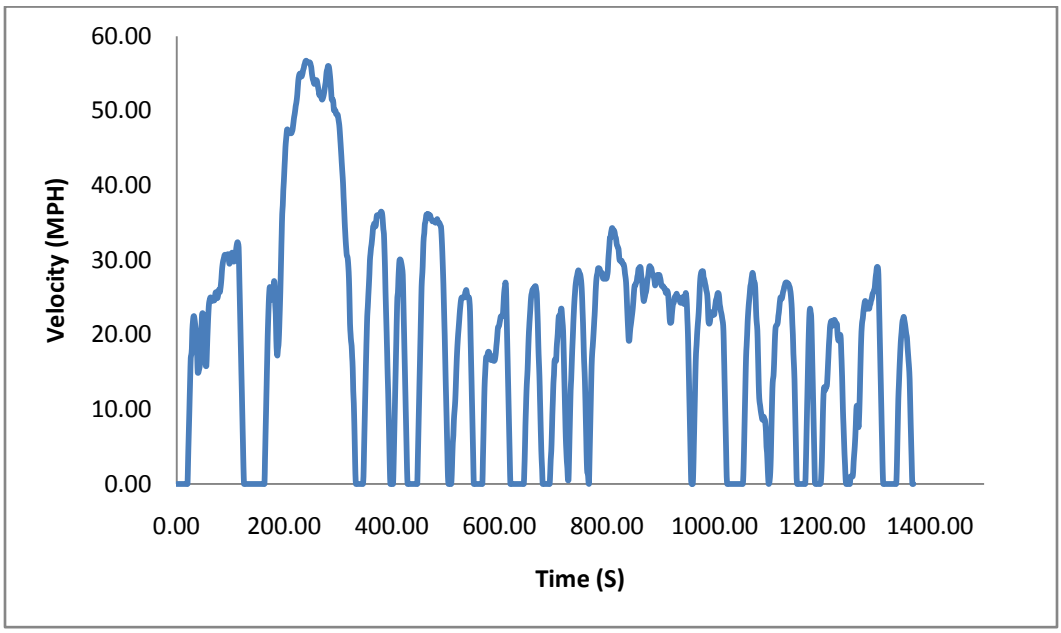

Figure 20: EPA Urban Dynamometer Driving Schedule

In order to represent the majority of Americans it was determined that the input flywheel should be capable of storing the energy necessary to run a vehicle through five driving schedules. Five schedules corresponded to 37.25 miles, which is the maximum number of miles driven on a daily basis by about seventy percent of the population.

After having specified a number of miles that would ideally be driven on flywheel energy, the calculations to determine this energy quantity could be performed. The following procedure is a detailed summary of how this calculation was performed.

A). Calculate the instantaneous acceleration from the EPA data

$$a(t) = \frac{V(t) - V(t-1)}{T_1 - T_0} \quad \textbf{(8)}$$

where a(t) is the instantaneous acceleration, V(t) is velocity at time step n, V(t-1) is velocity at time step (n-1), T_0 is time step n and T_1 is time step (n-1).

B). Calculating vehicle torque

$$T_v(t) = F_v(t) * r_v \quad \textbf{(9)}$$

where T_v (t) is the applied vehicle torque and r_V is the approximate radius of tire.

C). Calculating energy

$$E_v(t) = T_v(t) * \theta \quad \textbf{(10)}$$

where E_v(t) is energy required to apply torque for a set angular position and θ is the angular position.

Using this procedure with the UDDS data and the variables in Table 4, the force and torque required to move the vehicle throughout the cycle could be calculated. Figure 21 and Figure 22 are graphical representations of the vehicle force F_v(t) and the vehicle torque T_v(t). It can be seen on the graphs that the vehicle force and torque have both negative and positive values. These negative values correspond to vehicle deceleration. During typical vehicle operation this negative torque would be applied by using a friction brake, which in turn would result in energy loss. Since this project explores the possibility of capturing the energy lost due to braking and storing the energy in a flywheel, it was assumed that all of the energy required to slow the vehicle down could in fact be recaptured. Using equation (10) and the torque values shown in Figure 22 the energy required to drive the one city cycle was determined to be 3.71 MJ and the total energy to drive the five city cycles was found to be 18.5 MJ. It should be noted that these energy values do not take into account losses in the drive train or any other components of the vehicle. The only losses considered are those due to drag and friction.

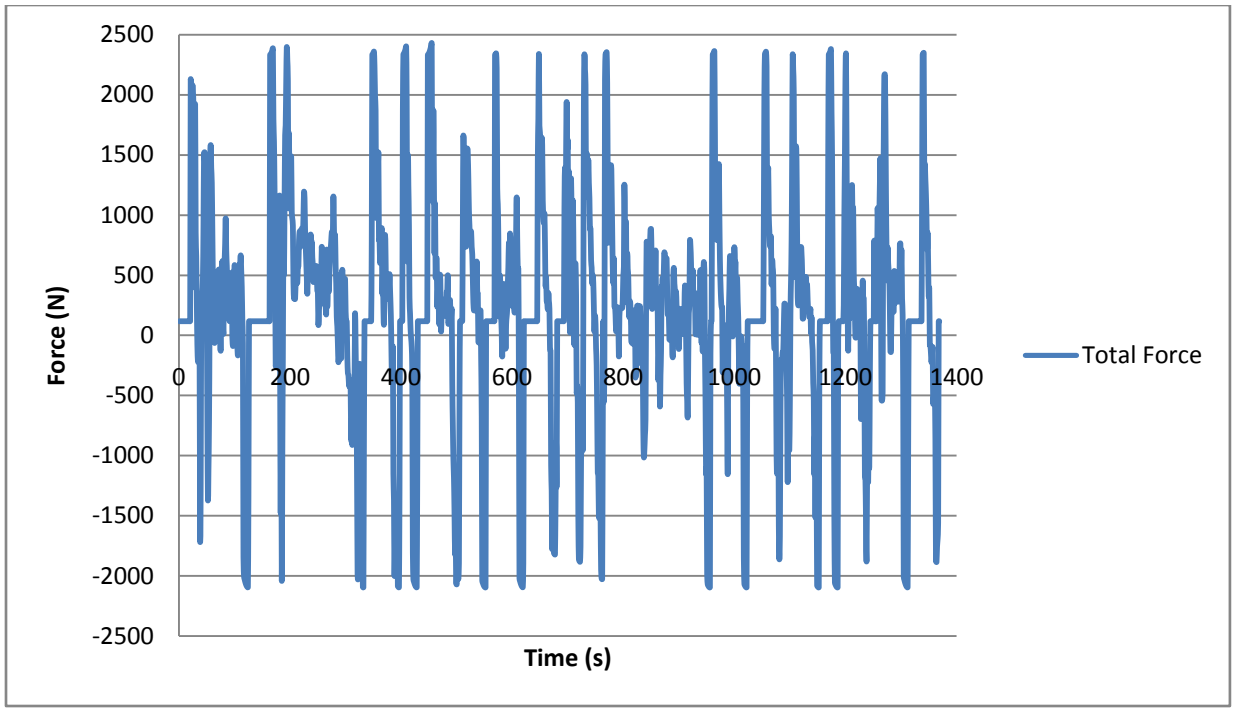

Figure 21: EPA UDD Force vs. Time

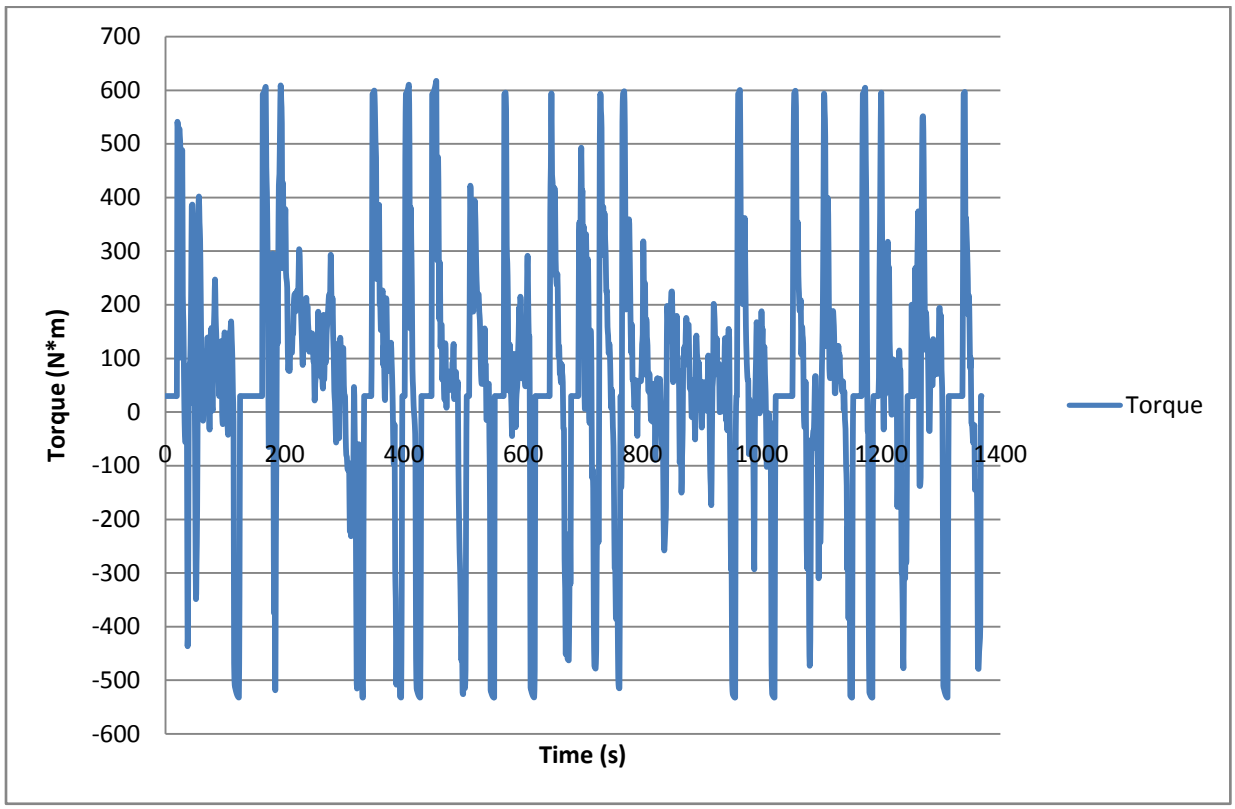

Figure 22: EPA UDD Torque vs. Time

Energy Storage of a Flywheel

In order to size the flywheel and choose a material, it was first necessary to examine the mathematics that governs its operation. The kinetic energy stored in a flywheel is described by (Bejan & Dincer & Rosen, 2002):

$$E_F = \frac{1}{2} * I_F * \omega_F^2 \quad \textbf{(11)}$$

Where E_f is the energy storage of the flywheel, I_f is the mass moment of inertia and ω_f is the angular velocity.

Assuming that the flywheel can be modeled as a uniform disk, the moment of inertia is defined as follows:

$$I_F = \frac{\pi}{2} * \rho_f * r_f^4 * t \quad \textbf{(12)}$$

Where ρ_f is the density of the flywheel material, r_f is the radius of the flywheel, and t is the thickness. Although it would be ideal for a flywheel of this nature to be geometrically optimized, it is not within the scope of this project to perform this task so in the calculations performed the flywheel will be modeled as a solid disk.

Combining equation (11) and (12) together gives an expression for the energy in terms of the angular velocity, density, radius and thickness.

$$E_F = \frac{\pi}{4} * \rho_f * r_f^4 * t * \omega_F^2 \quad \textbf{(13)}$$

Sizing a flywheel to store the desired amount of energy requires the appropriate balance of these variables. Previous work conducted on this project assigned an initial angular velocity of 50,000 RPM. Therefore, in order to obtain the desired energy storage the radius, thickness and material density can be varied.

One of the most important things to consider when choosing the geometry for the flywheel is the impact that each of these variables has on the overall stress. A spinning flywheel, illustrated in Figure 23, is subjected to both tangential and radial stresses, which can be calculated from the following equations. (Arora, 2004).

$$\sigma_T = \rho_f * \omega_f^2 * \frac{3 + v_f}{8} * [r_i^2 + r_0^2 + \frac{r_i^2 * r_0^2}{r^2} - \frac{1 + 3 * v_f}{3 + v_f} * r^2] \quad \textbf{(14)}$$

$$\sigma_r = \rho_f * \omega_f^2 * \frac{3 + v_f}{8} * [r_i^2 + r_0^2 - \frac{r_i^2 * r_0^2}{r^2} - r^2] \quad \textbf{(15)}$$

Where σ_T is the tangential stress, σ_r is the radial stress, ν_f is the poisons ratio, r_i is the inner radius, r_0 is the outer radius and r is the radius of interest.

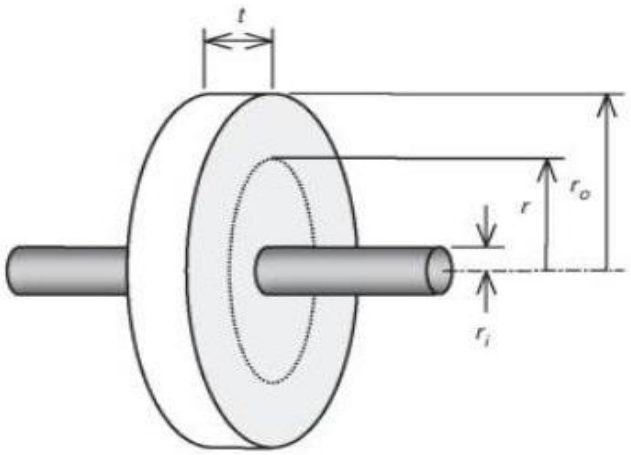

Figure 23: Flywheel with Indicated Radius

Examination of these stress equations shows that the maximum tangential and radial stresses occur close to the center of the flywheel, and decrease when approaching the outer edge. For the purpose of packaging in a standard passenger vehicle, the radius of the flywheel for this project was assigned a value of .250 m, which corresponds to .50 m diameter.

Equations (14) and (15) also show that the density of the material increases the stress proportionally. Before assigning a value to the density, a material had to be chosen. This material will be selected based upon two criteria: failure safety and energy density.

Safety Considerations

Two classes of materials will be examined for the flywheel that will be used in this project, these are isotropic and orthotropic. Isotropic materials are materials that behave the same way in all directions. Most metallic alloys and thermoset polymers are Isotropic. Orthotropic

materials are materials that have at least two orthogonal planes of symmetry. The material properties of an orthotropic material are independent of direction within each plane. Orthotropic materials include such things as carbon fiber and other reinforced polymers (Widmer & von Burg, 1995).

One of the most important parameters to consider when designing a flywheel is safety. Upon failure the fragmented components of a flywheel can be subjected to two types of motion, either translational, caused from tangential fracture or rotational, caused by hoop failure. Isotropic materials have a tendency to break into fragments and move in a strictly translational manner. Figure 24 is an illustration of an isotropic flywheel in a protective housing. From the schematic, it can be seen that when the fragment separates itself from the rotating flywheel it possesses rotational motion acquired from the spinning flywheel but it also acquires translational motion, which causes it to contact the housing.

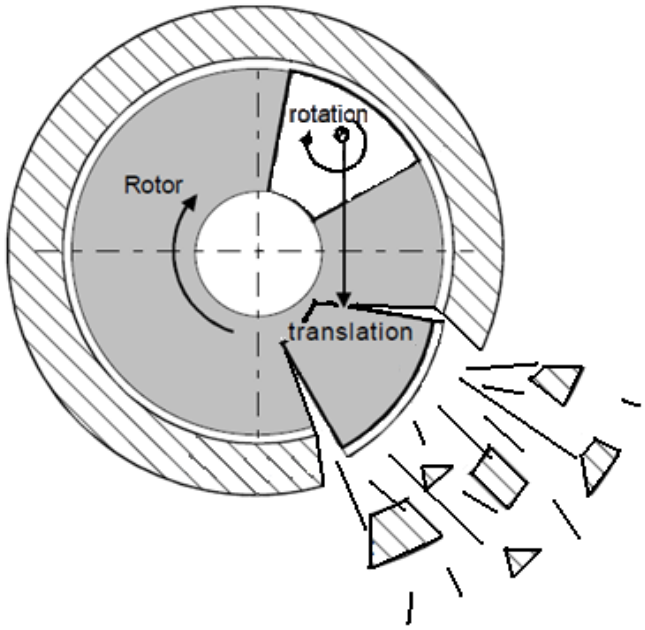

Figure 24: Failure of Isotropic Material (Edited, Source: Widmer & von Burg, 1995)

Because of the required high angular velocity of the flywheel, the corresponding translational speed of the projectiles will be substantial, and the housing used to stop the fragments before they damage their surroundings will need to be made of a material which is capable of absorbing large amounts of energy. However, this capability to absorb energy has the

potential negative side effect of either significantly increasing the weight or the size of the housing (Widmer & von Burg, 1995).

Orthotropic materials have significantly less negative side effects during failure because the stored energy is dissipated through primarily rotational motion. An orthotropic flywheel is usually constructed by winding a reinforced polymer around a central hub (Widmer & von Burg, 1995). As a result of its construction when the system fails, these fibers begin to unwind. As the fibers unwind, they rotate around the containment and create friction between the walls of the housing and the unwinding fibers. The frictional force begins to slow down the speed at which the system rotates and if the rotational speed is great enough, the heat created can potentially decompose the fibers. Because the housing will not be subject to an impact with a significant magnitude, it does not need to be capable of absorbing the same amount of energy as in the case of an isotropic material. Therefore, when designing the flywheel, a primary goal will be to provide a safe mode of failure for the system that minimizes or ideally eliminates the risk of tangential fracture (Widmer & von Burg, 1995).

Energy Density

Energy density is the amount of energy stored in a system per unit volume or mass, it is commonly referred to as specific energy when talking about energy per unit mass. In order to examine the specific energy of the system, the equations for flywheel kinetic energy and tensile stress are combined (Bejan et. al., 2002). The result is that the energy density of the system is proportional to the strength of the material divided by the density of the material (Arora, 2004).

$$\frac{E_f}{M_f} \propto \frac{\sigma}{\rho_f} \tag{16}$$

The energy density of the flywheel is therefore increased by maximizing the tensile strength of the material, while minimizing its density. Table 5, details some common isotropic and orthotropic materials along with their tensile strength, density and specific energy.

Table 5: Strength to Density Ratio of Common Materials

Material	Density (kg/m^3)	Tensile Strength (MPa)	Strength to Density Ratio (MJ/kg)
Steel	7800	1800	0.22
Aluminum Alloy	2700	600	0.22
Titanium	4500	1200	0.27
CFRP	1500	2400	1.60

Figure 25 is an Ashby chart which plots the density of the material along with its corresponding tensile strength. From the graph, it can be seen that the materials in the upper left hand region have the lowest density but highest tensile strength, and would therefore be most applicable for the flywheel.

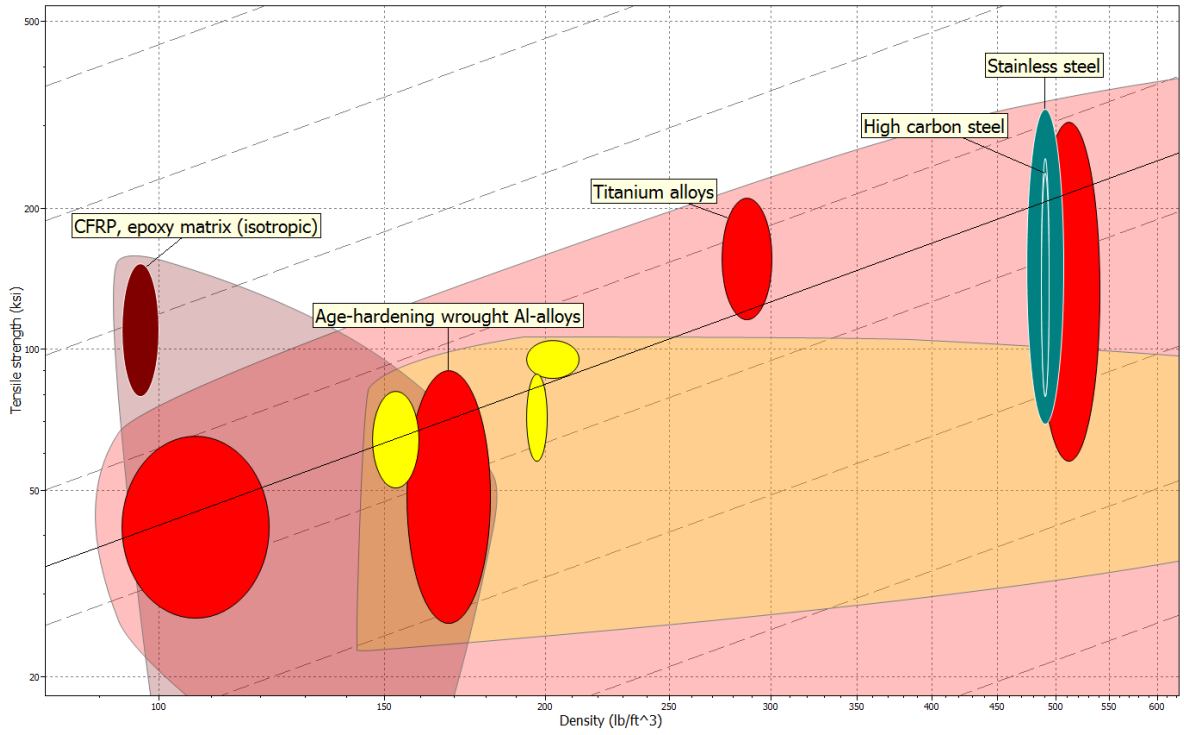

Figure 25: Ashby Chart for Density and Tensile Strength of Flywheel Materials

From the discussion presented above, it is clear that for the flywheel in this project an orthotropic material, carbon fiber, would be ideal because it has a larger energy density and will allow for a safer failure mode.

Summary of Geometric Modeling and Stress Distribution

Having assigned values for the energy storage and all of the variables present in equation (13) except for thickness, its value was easily determined. A summary of the flywheels dimensions are found in Table 6.

Table 6: Geometric Dimensions and Speed

Initial Spin Speed (ω_1) RPM	50000
Density of Material (ρ) kg/m^3	1500
Thickness (t) m	.127
Radius (r) m	.254
Volume (V) m^3	.026
Energy (E) MJ	18.532

In order to verify that these dimensions did not produce stresses in the flywheel that exceeded the yield strength of carbon fiber, the stress distribution throughout the flywheel was determined. This plot can be seen in Figure 26.

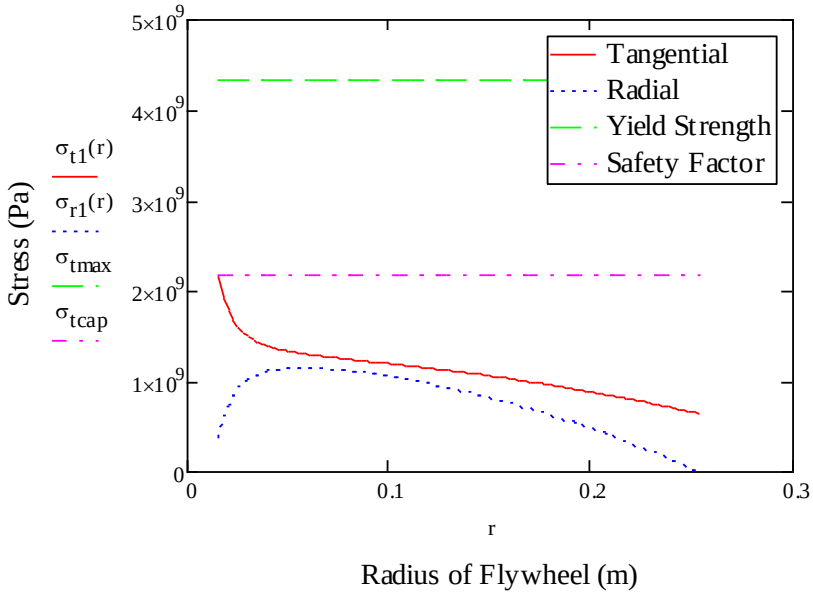

Figure 26: Stress Distribution Graph Input Flywheel

Figure 26 plots the yield strength of the material, the yield strength with a safety factor of two, and the stresses present within the material. It can be seen that these stresses do not exceed

the specified safety factor. This fact validates that the chosen geometry will safely produce the energy storage capabilities that are desired, while still being manageably packaged.

Spring design

Another main component of the system was the spring, as it transmitted torque through the system in both the generative and regenerative mode. The initial project description had no main design to the spring and how the transmittal of torque would happen. Multiple spring designs were considered to achieve certain constraints. These constraints were to have a modest packaging size, the ability to transmit torque in two directions, and a desired spring constant. Three existing designs were examined for their applicability, which were: solid bar, compression spring, and torsion spring. The solid bar was deemed unacceptable due to the large length and size of the bar to generate the desired spring constant. The compression spring was unacceptable because it needed large coils that did not satisfy the packaging constraint. Finally, the helical torsion spring could only transmit torque in one direction.

The implemented spring design was a variation on a torsion spring. The design used a series of bars connected around a circular cap to transfer torque by deflection in both bending and torsion. In order to validate calculations made by the MATLAB simulation discussed earlier, a spring constant of 685 N-m/rad was needed. To achieve this desired constant, the spring needed to deflect 110 degrees at the outer face of a xxx diameter spring cap. Due to the fact that the theoretical spring would be transmitting 1,000 lb-ft, or 1,356 N-m, it was important to minimize stresses while still getting the desired deflection of 110 degrees or, about 75 mm of displacement around the outer cap.

The first iteration, seen below in Figure 27, used two sets of rectangular bars set at different radii from the center. In order to find the effects of different size and shapes of bars each design was modeled using SolidWorks and analysis was run using COSMOSWorks Designer. The simulation was set up by fixing one cap in space and applying a torque around the other cap which had not been grounded. A summary of bar configuration, size, and results pertaining to deflection and stress can be seen in Table 7 and Table 8. The first column shows the overall diameter of the end cap. The second column states how many bars are in the configuration and their dimensions. The third and fourth columns show how far away the bars

are from the center of the cap and the overall length of the bars, respectively. Finally, the last two columns provide the displacement seen at the cap and the total stresses seen in the bars.

Figure 27: Spring iteration 1

Table 7: Staggered configurations

Cap Diameter	*Outer Bars*	*Inner Bars*	*Outer Bar Radius*	*Inner Bar Radius*	*Bar Length*	*Deflection at outer cap*	*Von-Mises Stress*
5	8 Rec (0.5 x 0.4)	6 Rec (0.5 x 0.4)	2	1	36	41.97 deg	6.344E8 N/m^2
4	8 Rec (0.5 x 0.4)	6 Rec (0.5 x 0.4)	1.5	0.5	36	33.40 deg	6.230E8 N/m^2
4	18 Rec (0.5 x 0.25)	5 Cir (0.5 dia)	1.5	0.5	36	41.67 deg	6.044E8 N/m^2
4	18 Rec (0.5 x 0.25)	5 Cir (0.5 dia)	1.5	0.5	48	55.82 deg	6.008E8 N/m^2

The first two iterations used a staggered configuration of rectangular bars with varying radii of the inner and outer bars. These changes showed very little change in the amount of deflection and stresses. Also, the deflection was well under the desired amount.

The third iteration, in Figure 28, made two major changes by replacing the inner rectangular bars with circular bars and significantly increasing the number of outer bars. This yielded about the same deflection and slightly less stresses. The fourth iteration simply added 12 inches to the length of the previous one to make an overall length of 48 inches. This change helped to increase the deflection as well as decrease the stress.

Figure 28: Spring iteration 3

After getting disappointing results from using staggered configuration the fifth iteration used a single set of 18 rectangular bars evenly spaced around the cap. This strategy drastically increased the stresses but allowed for acceptable displacements. This iteration was adjusted numerous times by reducing the number of bars and overall length to obtain the desired deflection of 110 degrees. The most effective way to increase deflection was to decrease bar thickness and increase length. The final bar thickness was chosen to be a standard metal thickness to simplify manufacturability. It was also seen that changing the cap and bar radius had minimal effects on deflection and were therefore minimized for more effective packaging and manufacturing. The final design can be seen in Figure 29.

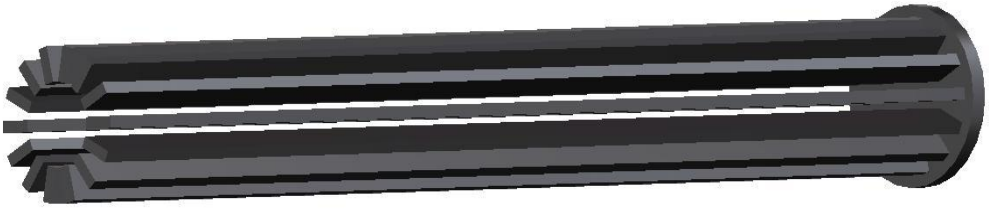

Figure 29: Final spring design

Table 8: Non-staggered configurations

Cap Diameter	*Outer Bars*	*Radius of Outer Bars*	*Bar Length*	*Deflection at outer cap*	*Von-Mises Stress*
3	18 Rec (0.5 x 0.2)	1	48	149.74 deg	1.620E9 N/m^2
3	15 Rec (0.5 x 0.2)	1	36	133.34 deg	1.807E9 N/m^2
3	15 Rec (0.6 x 0.2)	1	36	108.08 deg	1.489E9 N/m^2
3	14 Rec (0.6 x 0.2)	1	36	113.48 deg	1.583E9 N/m^2

Once the preferred displacement was reached, a material needed to be found that could safely withstand the stresses. As seen in Figure 30 below, the stresses are concentrated in the middle of each bar and peak at 1.583GPa. Alloy steel, AISI 9255 tempered and quenched was found to be a suitable material using CES EduPack.

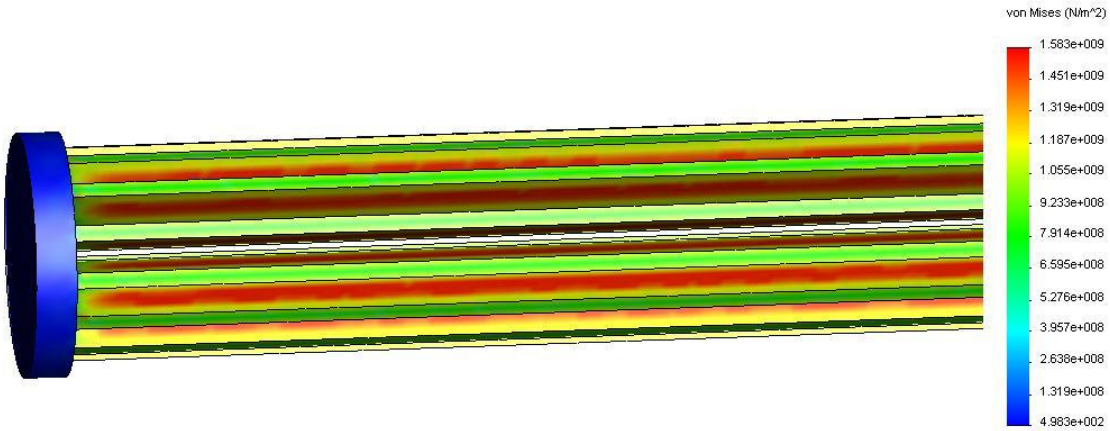

Figure 30: Stresses of final spring design

Theoretical spring design validation

In order to ensure the results calculated by COSMOSWorks Designer were accurate, a MathCAD file was used to calculate the deflection by hand. Using equations for the bending and torsional spring constant, the total spring constant could be found by summing the values and multiplying by the number if bars used in the design. These calculations, which can be seen in Appendix B, gave a spring constant of 639.121 Nm/rad. The total deflection was calculated by dividing the max torque by this k. The total angular deflection was 121.546 degrees. Finally, the percent error of the k value and deflection was found to be 6.6% and 7.1% respectively between the COSMOS and hand calculated results.

Prototype

Having identified the major components of the switch mode CVT as the input and output flywheels, clutch, anti-reverse ratchet, and the spring, the next step was to create a scaled down version of each component for a bench top prototype. After selecting the components and assembling the prototype, a data acquisition system was set up to monitor the prototype and pulse the clutch at the appropriate times. Finally, an enclosure was created for safety

considerations. The following is an in depth analysis of the individual parts that comprise the switch mode CVT.

Clutches

The clutch was the major limiting factor when designing the prototype. The only commercially available clutch with an engagement time fast enough to allow for a pulsing frequency of 20 Hertz was the EC75 electromechanical clutch manufactured by REELL. According to the manufacturer's specifications, the clutch can engage in as little as three milliseconds at a maximum speed of 1400 RPM. Figure 31 is a graphical representation of the clutch's engagement time at varying speeds. Although the speed of the clutch engagement was adequate for the project, the maximum torque transfer through the clutch was limited to 75 in-lb (6.779 N-m).

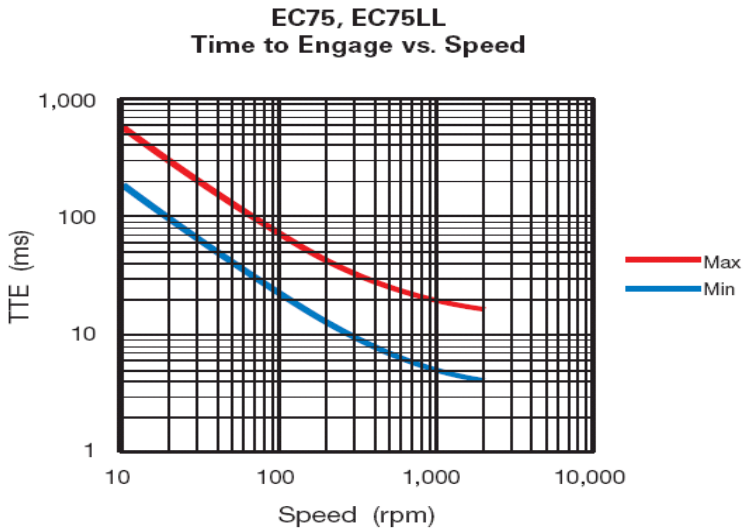

Figure 31: Engagement Times of Clutch

Flywheels

The input flywheel was scaled down based upon energy storage. The full scale input flywheel could store 18.53 MJ of energy, but since the clutches could only handle a velocity of 1400 rpm the system had to be scaled down accordingly. Using an angular velocity of 1400 RPM, the geometry was chosen so that at maximum speed the flywheel could store 1850 J of energy. The output flywheel was sized based upon its mass and moment of inertia. This flywheel was modeled as a vehicle and for that reason it was desired that during operation the vehicle be

able to achieve an appropriate acceleration value of 3.126 m/s^2. The moment of inertia of the output flywheel was determined to be 0.116 m^2-kg and the appropriate geometry to achieve this value was chosen. Although it was discussed earlier that an orthotropic material, like carbon fiber, would be much more suited for a flywheel, its cost made it impractical for application within this prototype. For that reason, a low cost steel was chosen. In addition, steel was easier to manufacture. A summary of the dimensions and properties of the input flywheel can be seen in Table 9.

Table 9: Input and Output Flywheel Dimensions

Variable	Input Flywheel	Output Flywheel
Outer Radius (in)	5.000	4.000
Inner Radius (in)	0.375	0.375
Thickness (in)	2.250	3.000
Mass (Kg)	22.587	19.3
Moment of Inertia (m^2-kg)	0.182	.116

Stresses within Flywheels

Having specified the geometry and angular velocity of the flywheels, the stresses found within each could be calculated. Figure 32 shows the tangential and radial stress distribution found within the input and output flywheels. These graphs were created by using equations (14) and (15). Also contained on the graph is the yield strength of steel with a very large safety factor of 225.

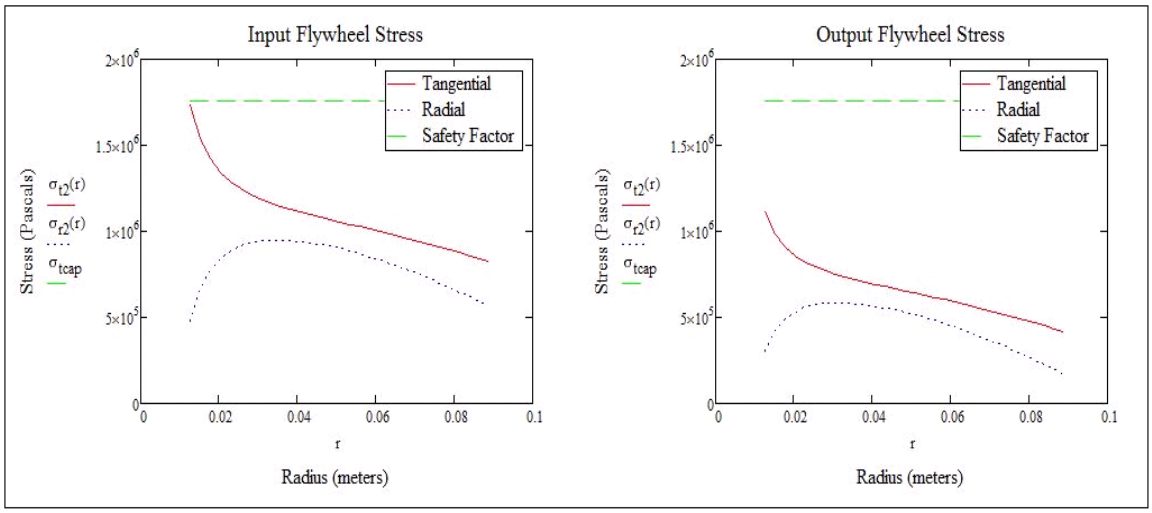

Figure 32: Stresses Within the Input and Output Flywheels

Spring Assembly Design

The spring was designed to achieve its maximum deflection of 110 degrees when subjected to a torque value of 75 in-lb. In addition, it was desirable to keep the stresses within the assembly to a minimum. The spring for the prototype was a modification of the theoretical design previously discussed. However, material selection and manufacturability played an important role.

End caps were created to locate the bars of the spring and they were made out of two pieces, an inner and outer piece that created a seal when pressed together. The caps were made of aluminum and had a pattern of three wedges at 120° intervals with one of the corners of each wedge facing the center of the cap. One piece was the milled out profile of the face of these wedges and the second was the inverse of the first piece. This was done so that these pieces can be press fit into one another, much like puzzle pieces, and provide a strong clamp over the spring beams while keeping the beams equidistant from each other. In addition, three tapped holes were made on the face of both end caps to be used for cap screws to ensure that the beams and caps remained intact under operation of the transmission. Figure 33 is an illustration of the two components used to make the end cap.

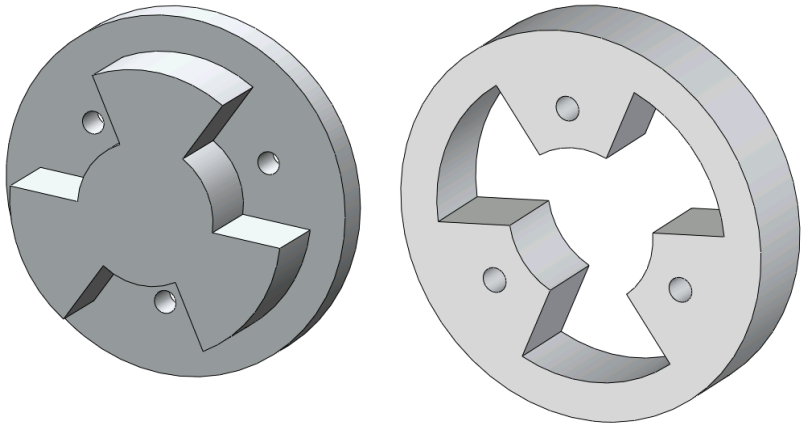

Figure 33: Spring Cap Components

The width and thickness of the bars were selected based on commercially available products. The material chosen for the spring was 4130 sheet steel, with a thickness of .040 inches. The length of the bars was chosen to be 21 inches overall and the width was chosen to be .5 inches. The spring bars were created by purchasing 36" by 6" sheets of 4130 steel and cutting

six pieces to size by using a metal shear. The six cut steel pieces were placed in a jig comprised of two pieces of lower grade steel and those two pieces were welded together, effectively clamping down the spring beams and preventing movement during heat treatment. The clamped and contained parts were then sent to Bodycote to be heat treated. The spring bars were placed in between the pieces of the end cap while a press forced the two together, creating a compression fit. The CAD model of the spring can be seen in Figure 34 and the manufactured spring is shown in Figure 35.

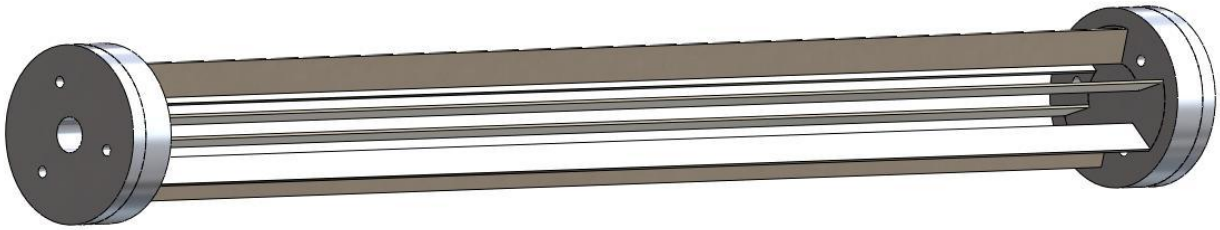

Figure 34: Spring CAD Model

Figure 35: Manufactured Spring

In order to validate the design FEA was performed on the entire assembly. The displacement under maximum loading conditions and the stress distribution were determined. The results obtained were verified by calculating the combined deflection due to the bending and torsion of the assembly. Figure 36 and Figure 37 show the deflection and stress, respectively.

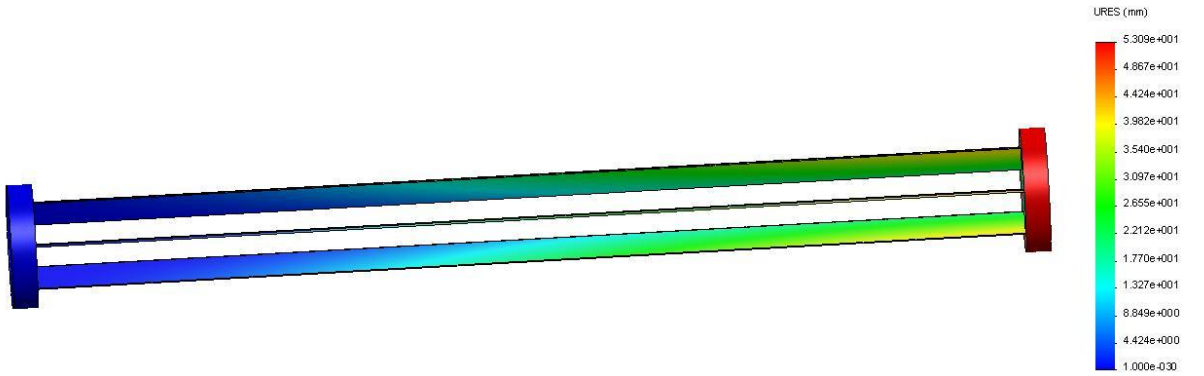

Figure 36: Deflection in Spring

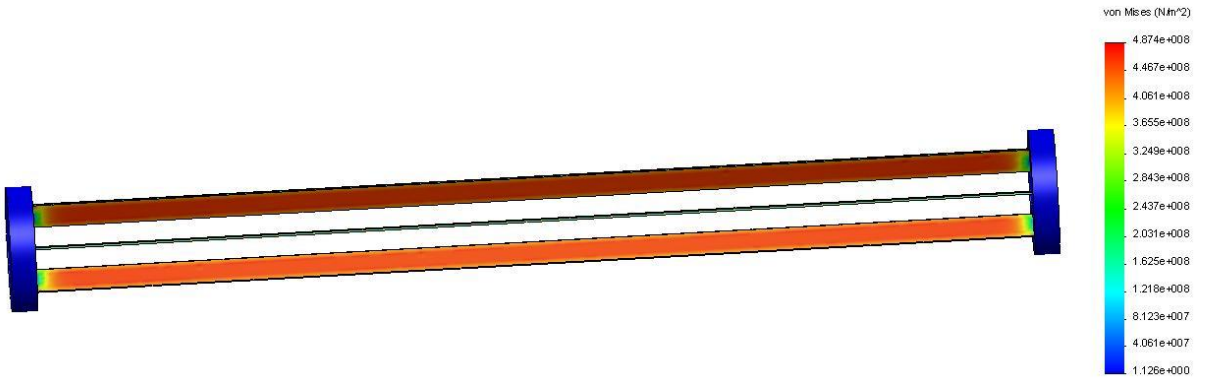

Figure 37: Stresses in Spring

Mating the Flywheels to Respective Shafts

The input and output flywheels were connected to their respective shafts with shaft locking collars. The collars are hollow rings, which fit over the input and output shafts and inside the flywheels. The collars have socket head cap screws attached to their face, and as the screws are tightened, the thickness of the collar decreases which in turn expands the circumference of the collar. This creates a strong, uniform connection between the shaft and flywheel. The input flywheel has two collars attached, in order to ensure that it remained balanced during operation. The output flywheel only has one collar due to manufacturing difficulties. Figure 38 is a picture of the shaft locking collar used in the transmission.

Figure 38: Shaft Locking Collar

Bearings

Two types of bearing were needed for this project. The first bearing was a one-way locking bearing, which allowed torque to be transmitted in one direction while freewheeling in the other direction. The 1/2” locking bearings chosen could handle well over 75 in-lb of torque and 1400 rpm and had a minimal inertial effect on the system. In addition to these locking bearings a set of 3/4" ball bearings were used to allow for the rotation of the input and output flywheel.

Supports and Base

A series of supports were created to suspend and attach the various components of the system to the base plate. A total of seven supports were manufactured, four of which had a 3/4” bearing press fit into them and were positioned on each side of the flywheel, two of them were bored out to accommodate the clutches and one was created to house the grounded locking bearing. A base plate was made out of aluminum and a series of slots were cut. The location of these slots corresponds to the desired placement of each support. When each support was bolted in, the slots allowed for small amounts of movement which helped to axially align the assembly. Because a fair amount of precision was needed when making these components the parts were imported to a CAM software and the created files were then sent to the HAAS Mini Mill and HAAS VF-4 milling machines. The automated milling ensured that every piece created by the mills retained dimensions with a precision of up to four thousandths of an inch.

Blast Shield

To prevent the flywheels and spring from causing destruction to outside sources in a possible failure situation, a box comprised of 1/2” lexan and plywood was created. The front and top of the box are lexan, the back and sides are plywood, and a piano hinge is used to allow the

top of the box to lift up for inspection and adjustments of the flywheel. An opening was left on the back of the box to allow access to the encoders and clutches.

Data Acquisition and Counting

In order to obtain experimental data from the prototype a data acquisition system was purchased and installed. This system had two primary functions, the first was to power and pulse the clutch and the second was to record and analyze data from the system. A summary and description of the major components required to perform both primary tasks is contained below.

Powering the Clutch

The National Instruments PCI 6220 was used to pulse the clutch. The PCI 6220 is a multifunction M series data acquisition card, used for cost sensitive applications (NI, 2009). This card was chosen because it contained digital outputs, a 32 bit counter and digital triggering. The only problem with the card was that the maximum output voltage was 5V while the clutch required 24 V. In order to compensate for this difference a simple circuit was setup utilizing an outside 24 V power supply and a transistor. The 5V power supply from the DAQ would open and close the main circuit, which in turn would power the clutch. A schematic of the wiring diagram can be seen in Figure 39. Additionally, a lab view file was setup to control the rate at which the clutch was pulsed. An illustration of both the front panel and block diagram for the program can be found within Appendix C.

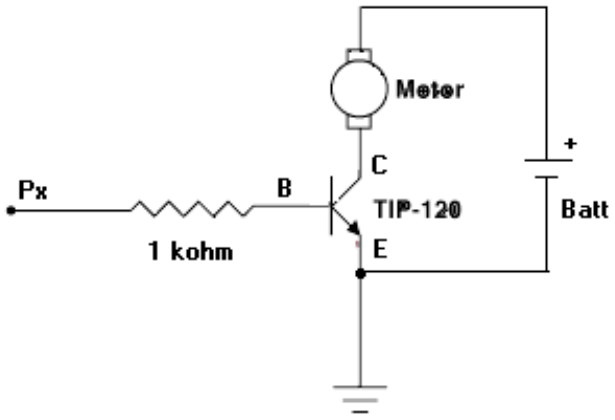

Figure 39: Wiring Schematic (UMN, 2009)

Recording and Analyzing Data

In order to monitor the position of the various shafts in the system, a series of rotary encoders were installed. The input and output shafts were tracked by two Digikey AMT 102 encoders, seen in Figure 40. The maximum bore size of these encoders was .25 inches, so the shafts were turned down to that diameter. These encoders could read data at a maximum rate of 2400 pulses per revolution. The position of the intermediate shaft was tracked with the US Digital HB6M hollow bore encoder, seen in Figure 41. The bore diameter of the encoder was .5 inches so no modifications needed to be made to the shaft. This encoder could read at a maximum rate of 10,000 pulses per revolution. It was necessary to use a faster reading encoder for the intermediate shaft because of the rapid changes in position caused by the engagement of the clutch. Additionally, this encoder contained a noise filter, which helped to eliminate error in the data.

Figure 40: Digikey Encoder (Digikey, 2009)

Figure 41: US Digital Encoder (US Digital, 2009)

The National Instruments PCI 6601 counter card was used to receive data from the rotary encoders. The PCI-6601 is a timing and digital I/O device that offers four 32-bit counter/timers and up to 32 lines of TTL/CMOS-compatible digital I/O (NI, 2009). The main purpose of this device was to analyze and interpret position changes from the rotary encoders attached to the system. A lab view file was setup to receive and analyze the data from the counter card, and then output the information to a Microsoft Excel file. An illustration of both the front panel and block diagram for the program can be found within Appendix D. It should also be noted that due to the large number of signals being processed and sent by the three encoders and clutch program, two computers were utilized to run the data acquisition system. Originally, a single computer was used to process all the incoming data; however, that overwhelmed the system and slowed the internal counter. For that reason, one computer was used to collect data from each of the encoders, while the other was used to run the clutch using program.

Summary of System

After having sized all of the components, the full CAD model was assembled. A schematic of the model with the major components labeled can be seen Figure 42. As illustrated in the figure, the input flywheel is attached to the input shaft with shaft locking collars. Ball bearings were placed in the flywheel supports, to suspend the flywheel while still allowing it to spin with minimal friction. The intermediate shaft connects the input of the system to the spring. Two sprag bearings, located on both sides of the intermediate shaft, enabled it to transfer torque in one direction while free-wheeling in the other. One sprag bearing was grounded to prevent the spring from transferring torque in the opposite direction. All of the components were elevated with supports, and the supports were bolted to the base. To ensure proper alignment, slots were created in the base that allowed for the supports to be moved axially.

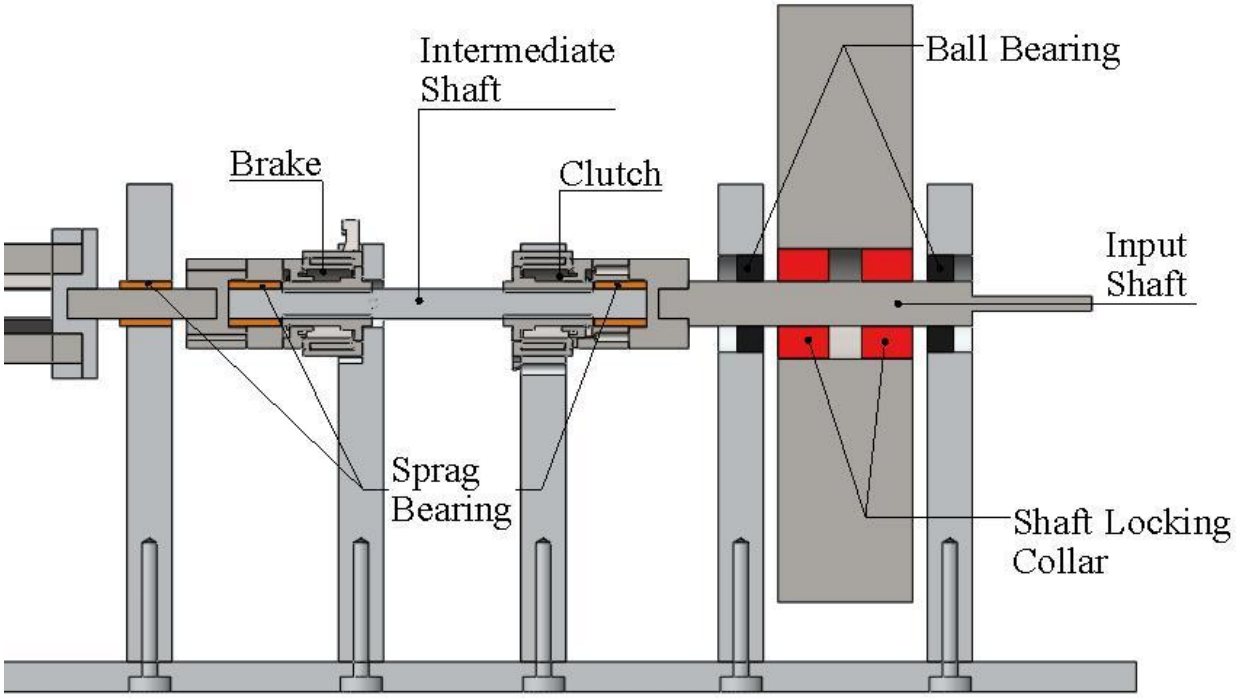

Figure 42: Cross-sectional view of CAD model

The final prototype, seen in Figure 44 came out very similar to the CAD model, see in Figure 43. The only real variation between the two assemblies came about because of manufacturing difficulties. The main discrepancies were found within the flywheels. The input flywheel had three, 0.5" holes drilled at two different radii. These holes were necessary to allow the flywheel to be placed on a lathe chuck to start turning and facing the flywheel. The facing was the hardest part to accomplish as passes needed to be first made from the outer radius to a position next to the nuts holding down the bolts. Once the desired thickness was achieved, the bolts were placed into the outer holes, and facing on the inner portion of the flywheel could be complete. The output flywheel had the same problems for turning down the outside radius. However, the thickness was cut down by using a manual mill as the flywheel could fit within a vice. The next section of the report looks at the results obtained from experimental testing.

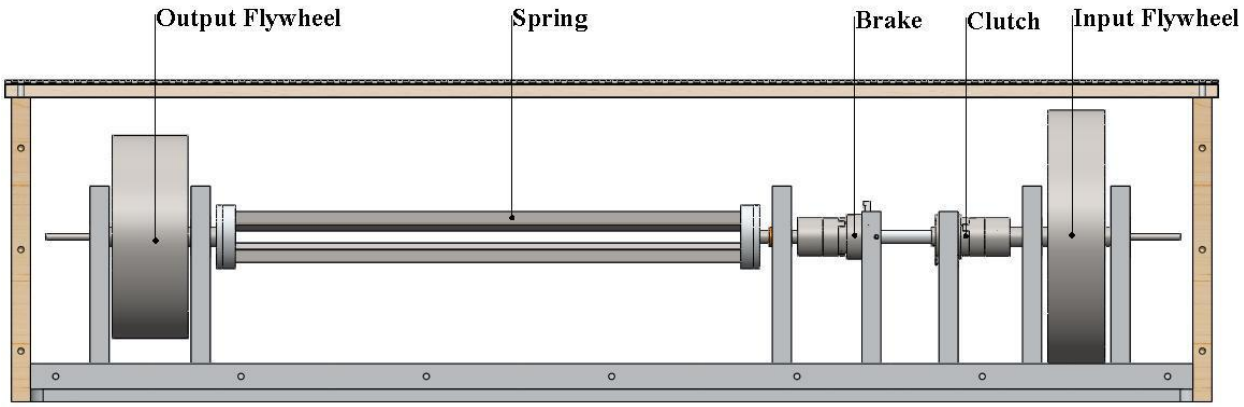

Figure 43: Full CAD Model

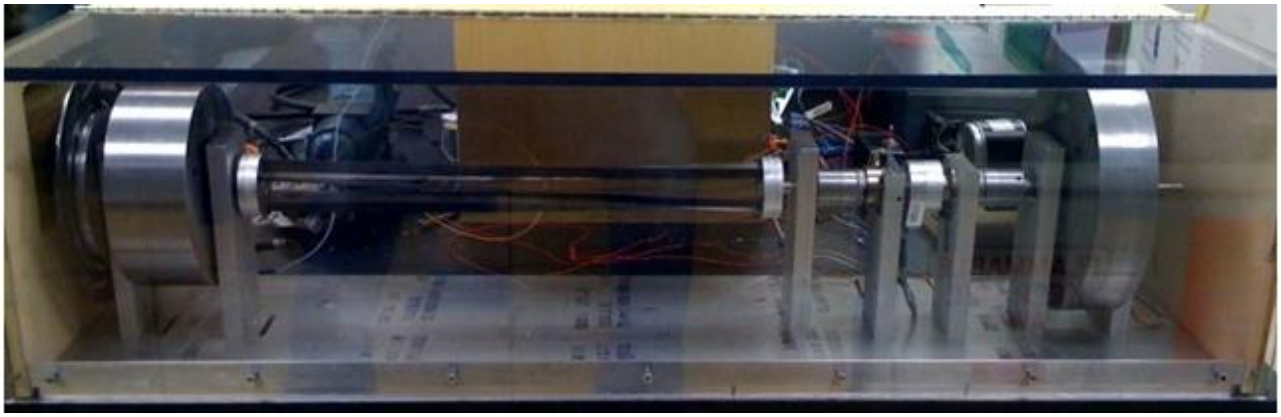

Figure 44: Benchtop Prototype

Results

This section is a summary of the experimental data obtained from the working prototype. It is broken down into three sections. The first is verification of the theoretical spring rate. The second looks at quantifying the frictional losses found in the input and output flywheels. The final section contains data obtained from testing the prototype at various speeds. Contained within each section is a description of how data was gathered, along with the results obtained.

Spring Rate

The spring rate of the prototype spring was calculated using a spring scale attached to the output flywheel. The spring scale was attached to the flywheel at a radius of 2.25 in (0.057 meters) and a force of 6 lbf (26.689 newtons) was applied upward. This force corresponded to an angular deflection of 17 degrees or 0.279 radians of the flywheel. Using the radius and force to calculate the torque applied, 1.52 Nm, the relationship of torque divided by angular deflection was used to solve for the spring constant. The resulting k value was 5.12 Nm/rad. The following section will discuss the results in further detail and explore possible causes for error.

Frictional Losses

The frictional losses in the input and output flywheel were calculated by spinning the flywheels to a certain speed and allowing them to come to a stop. Using the position data obtained from the encoders, the velocity of the flywheels was calculated. Figure 45 and Figure 46 are graphs of the input and output velocities, respectively, starting from their maximum speed and going to zero. Equations were formulated by fitting a trendline to both velocity plots. The formulation of these trendlines will be discussed in the following section. It should be noted that the following plots were created from two separate trials run.

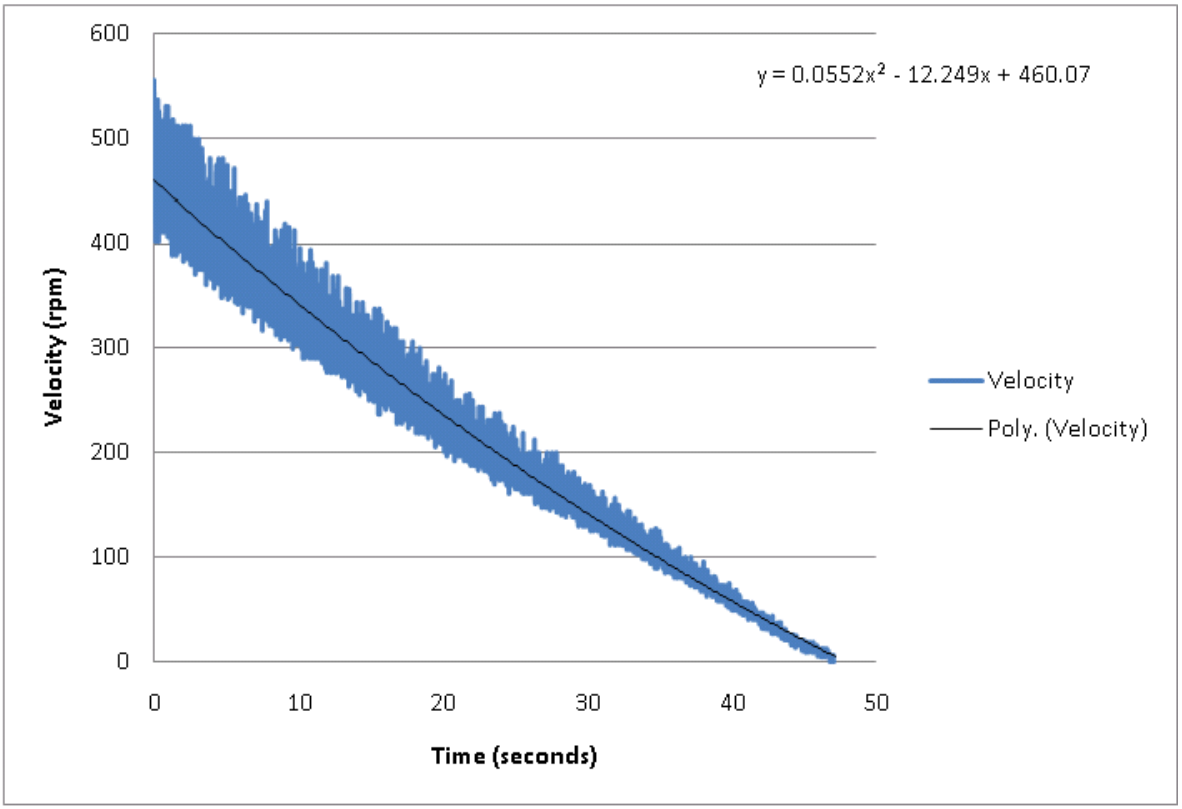

Figure 45: Frictional Loss of Input Flywheel

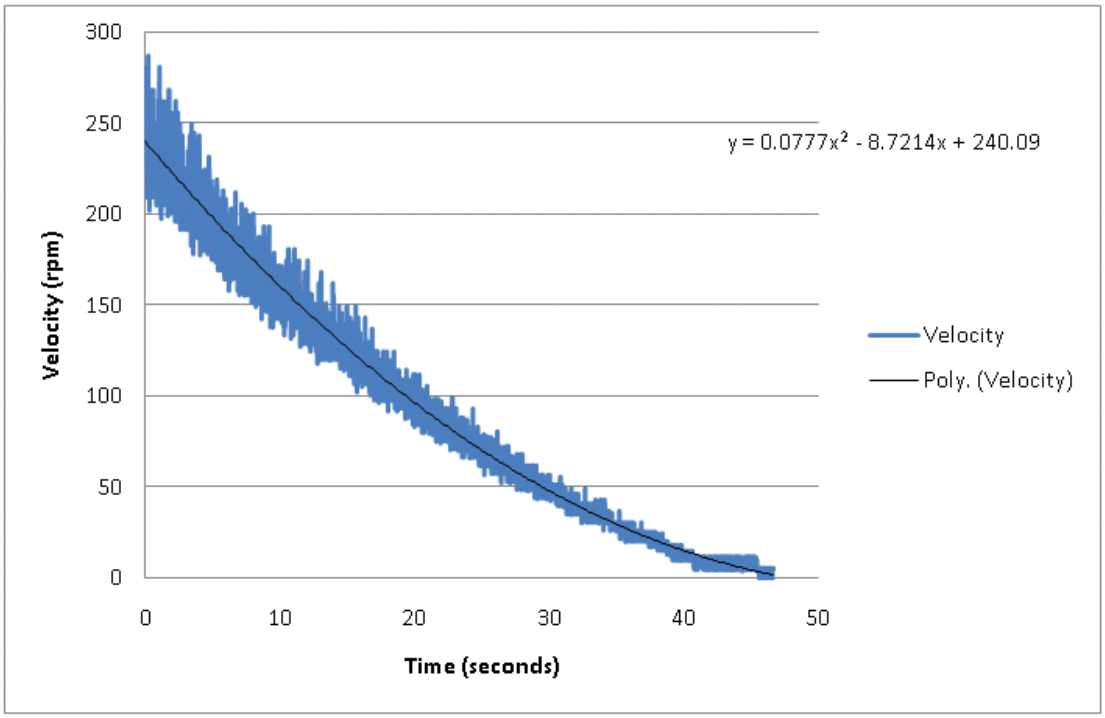

Figure 46: Frictional Loss of Output Flywheel

Prototype Testing

In order to obtain experimental data from the prototype a testing procedure was created and employed. This testing procedure is summarized below:

- All three encoders turned on to track the position of the various components of the system.
- Input flywheel spun to the desired angular velocity using a friction drive wheel powered by a 24 volt DC motor.
- Clutch pulsing program started once input flywheel achieved desired velocity.

Using this testing procedure data was obtained at varying angular velocities of the input flywheel. A summary of the data obtained is detailed below.

250 RPM Trial

The first set of trial data was collected using an input speed of 250 rpm and a clutch pulsing frequency of 5 Hz, which corresponds to a duty ratio of 0.3. Looking at the data obtained from the input encoder, a position plot, seen in Figure 47, was generated. Then, by taking the derivative of the position data, a velocity plot was created. However, it was discovered that the encoder is very susceptible to noise. In order to minimize the error in the data set, a moving average was applied. Figure 48 is a graph of the velocity with the applied moving average.

Using the same procedure, position and velocity graphs were obtained for the intermediate shaft and output flywheel. The intermediate position and velocity graphs are seen in Figure 49 and Figure 50, respectively. The output flywheel position and velocity graphs are seen in Figure 51 and Figure 52, respectively.

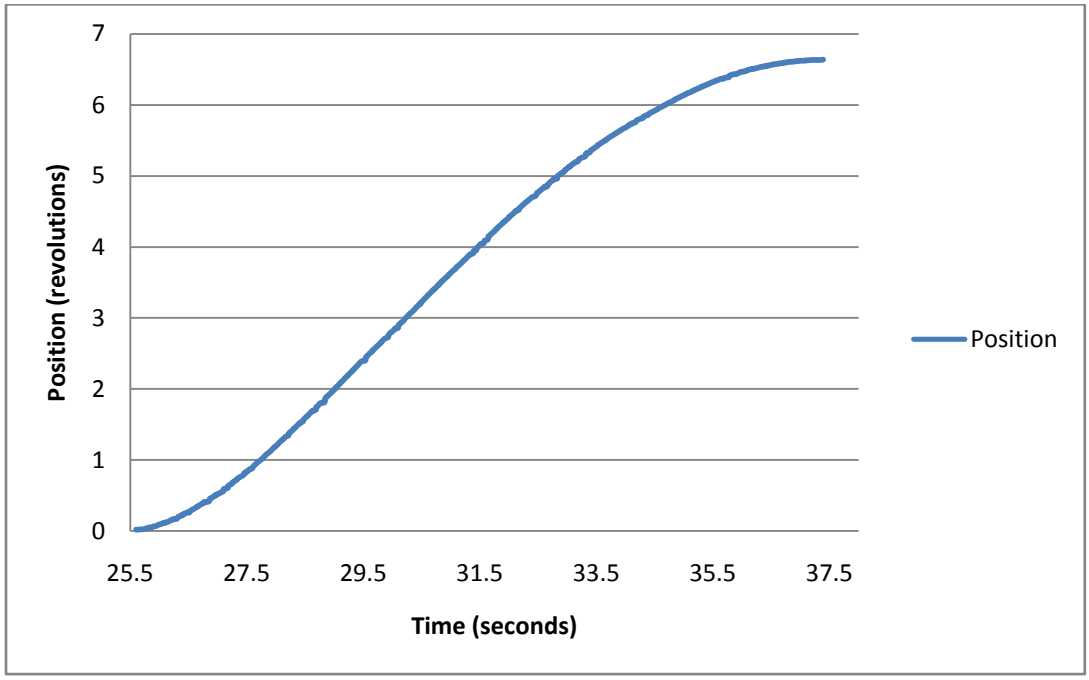

Figure 47: Input Flywheel Position Graph

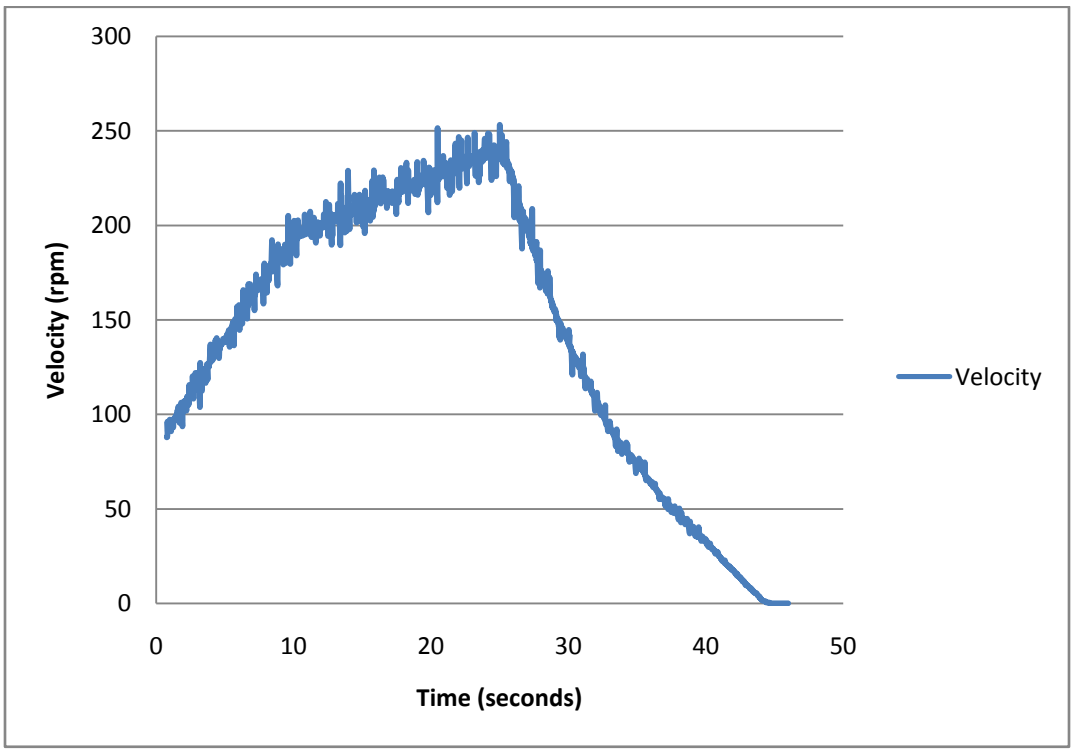

Figure 48: Input Flywheel Velocity Graph

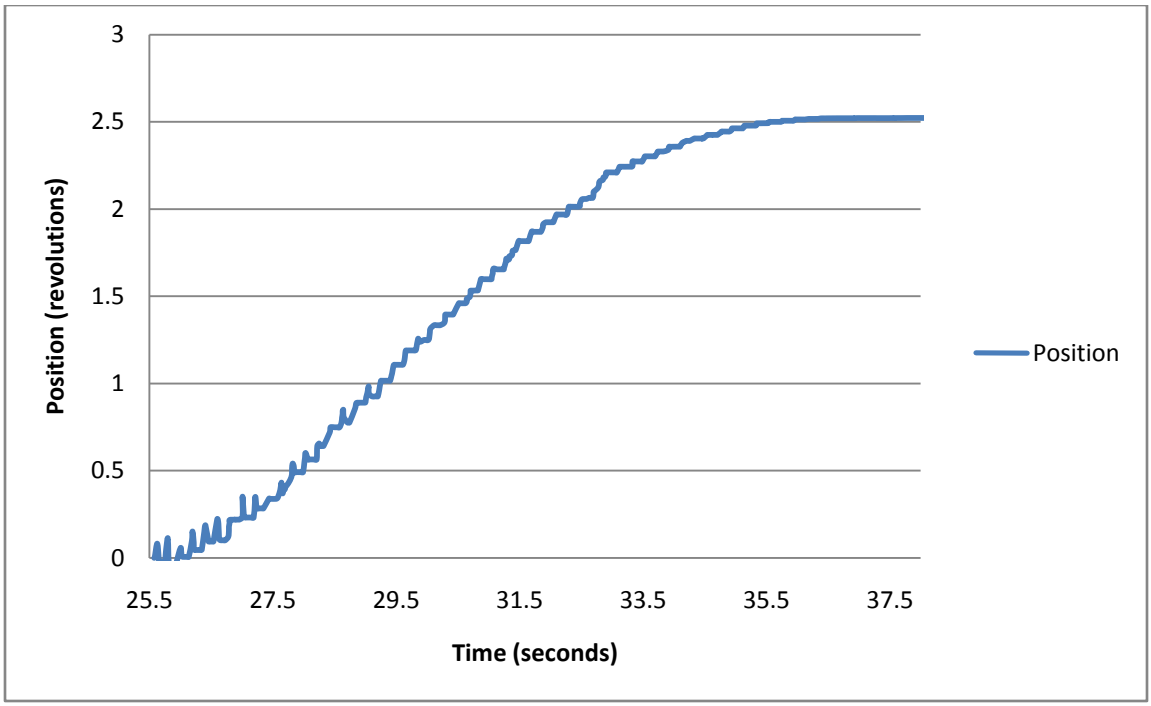

Figure 49: Intermediate Shaft Position Graph

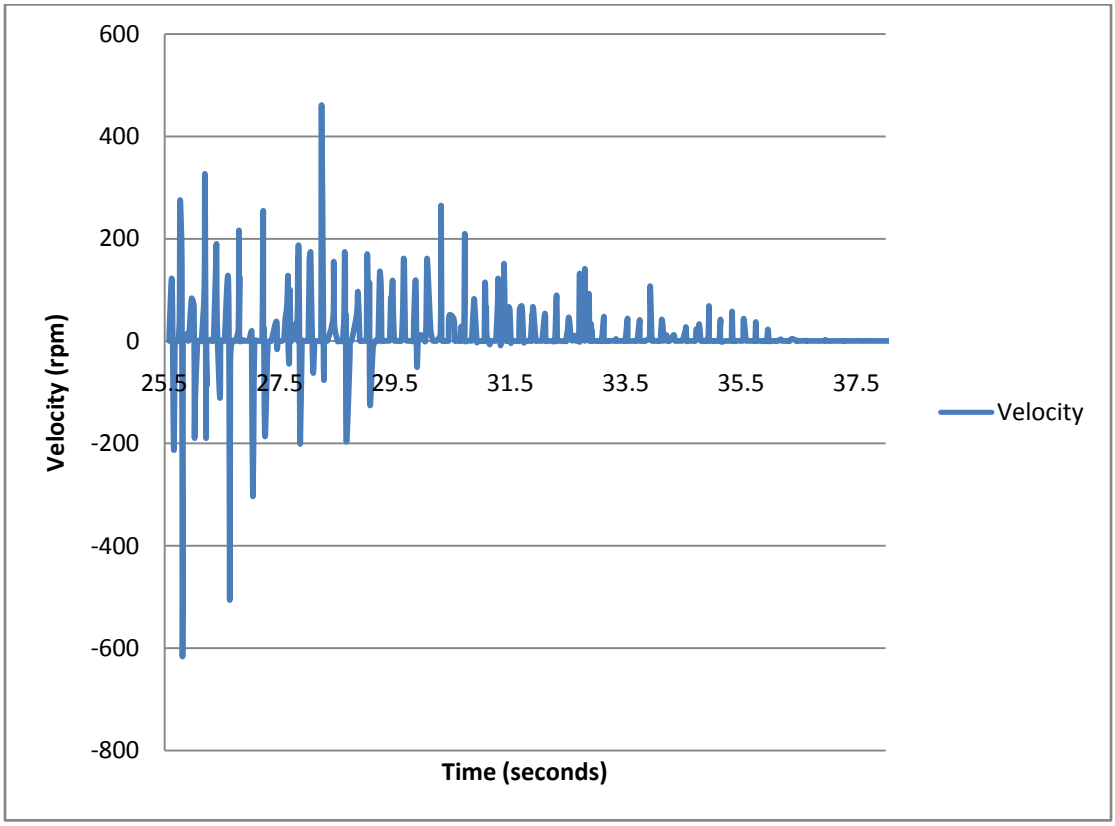

Figure 50: Intermediate Shaft Velocity Graph

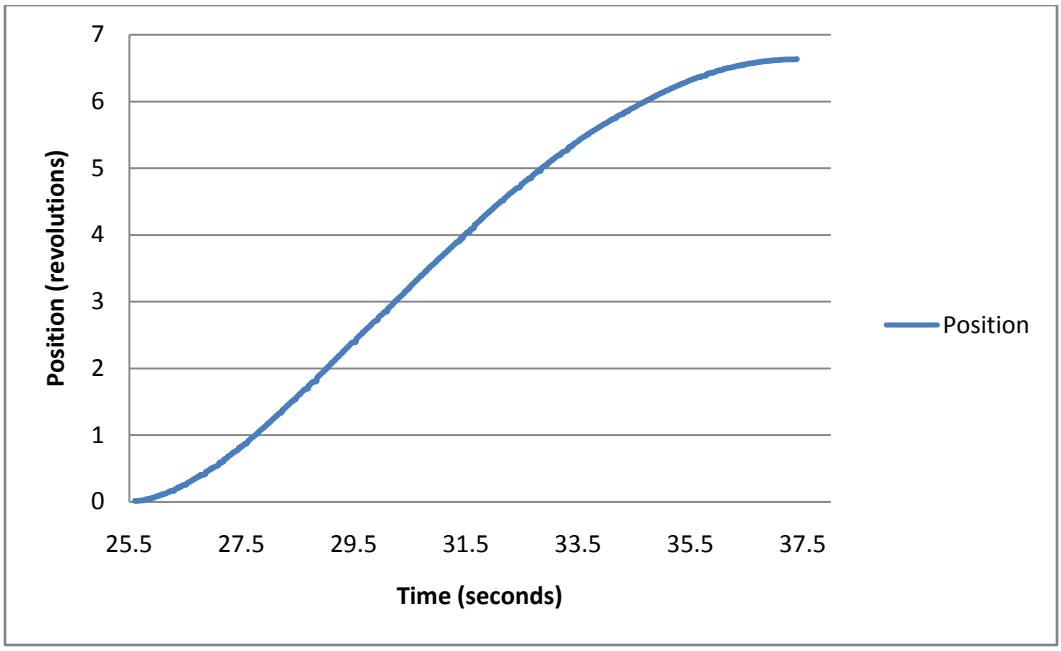

Figure 51: Output Flywheel Position Graph

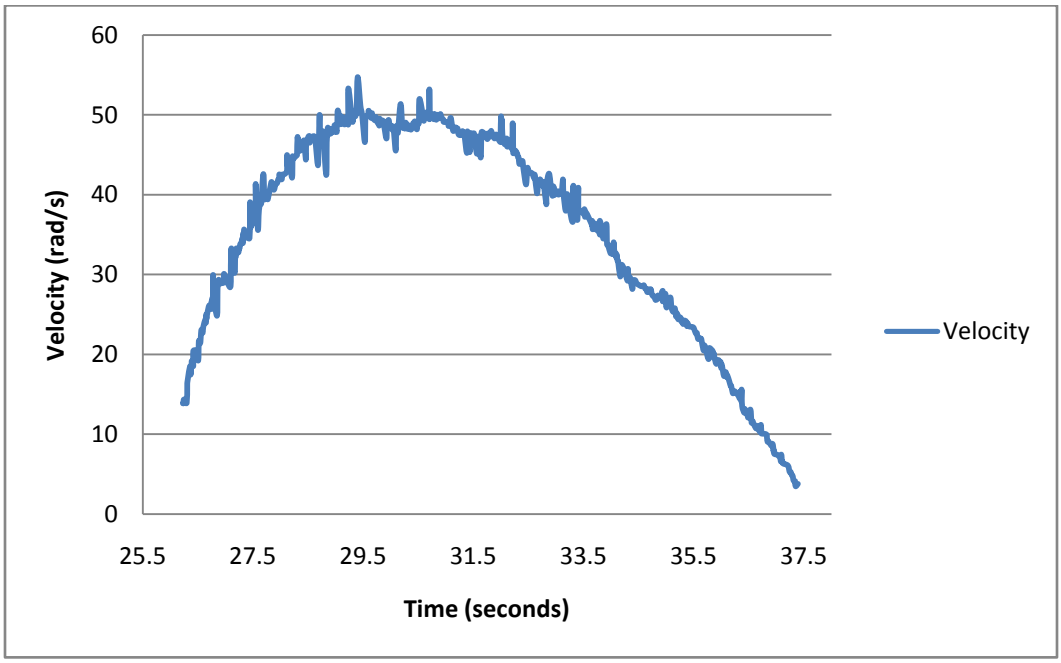

Figure 52: Output Flywheel Velocity Graph

500 RPM Trial

The second set of trial data was collected using an input speed of 500 rpm and a clutch frequency of 5 Hz. Looking at the data obtained from the input encoder, a position plot, seen in Figure 53, was generated. Then, by taking the derivative of the position data, a velocity plot was

created. In order to minimize the error in the data set, a moving average was applied. Figure 54Figure 54 is a graph of the velocity with the applied moving average.

Using the same procedure, position and velocity graphs were obtained for the intermediate shaft and output flywheel. The intermediate position and velocity graphs are seen in Figure 55 and Figure 56, respectively. The output flywheel position and velocity graphs are seen in Figure 57 and Figure 58, respectively.

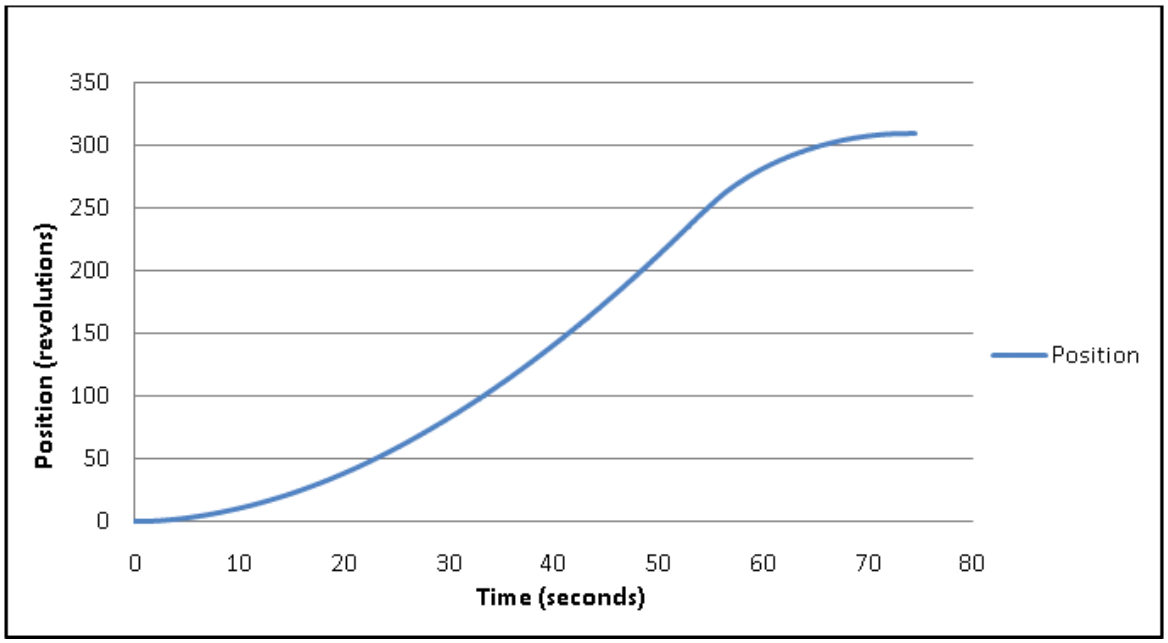

Figure 53: Input Flywheel Position Graph - 500 rpm

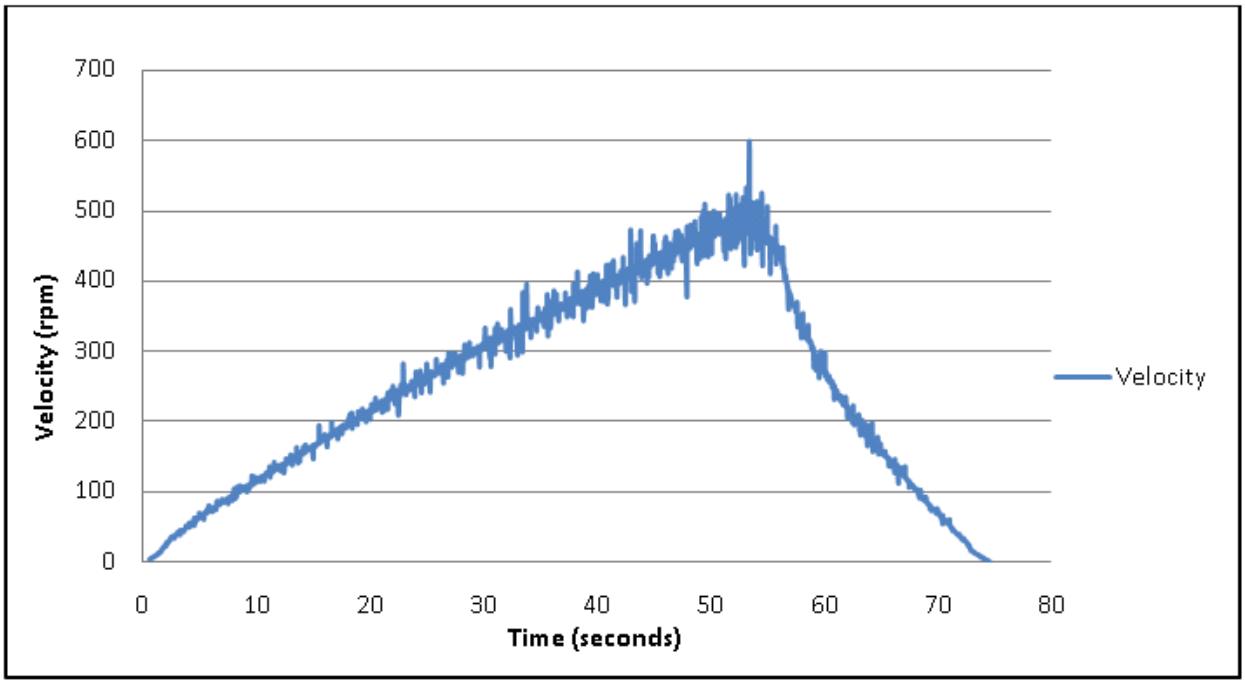

Figure 54: Input Flywheel Velocity Graph - 500 rpm

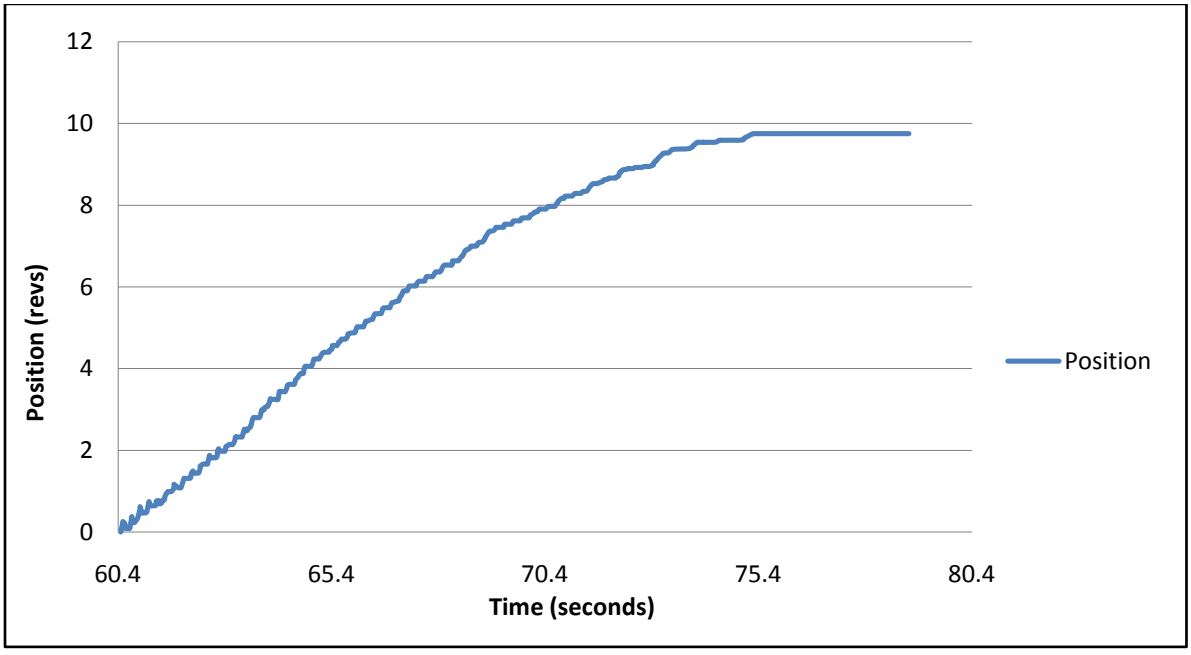

Figure 55: Intermediate Shaft Position Graph - 500 rpm

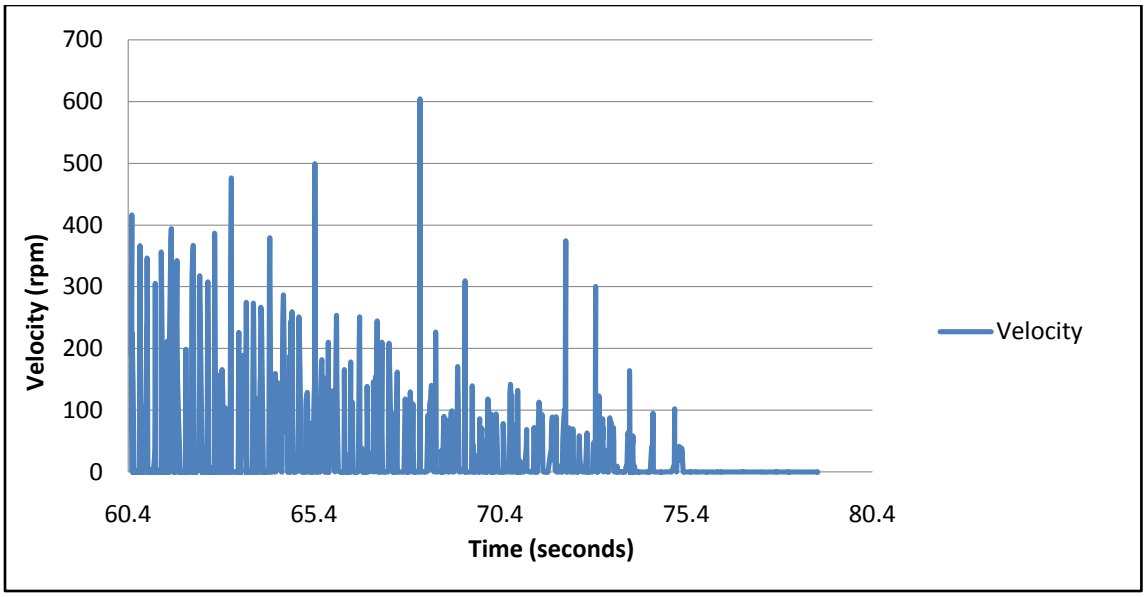

Figure 56: Intermediate Shaft Velocity Graph - 500 rpm

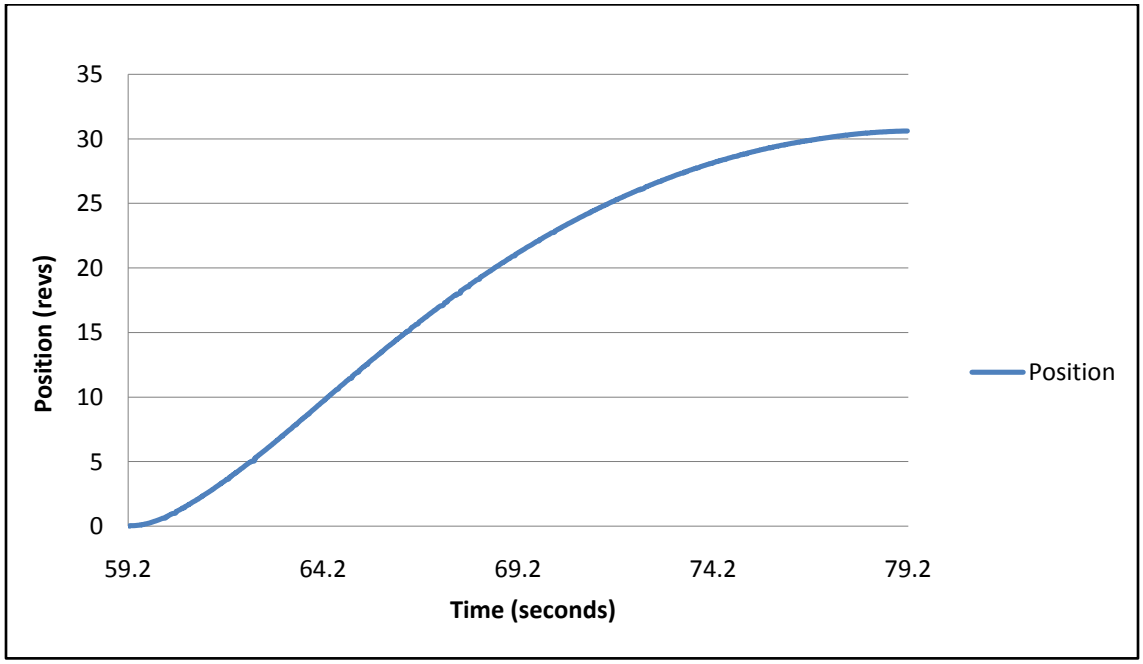

Figure 57: Output Flywheel Position Graph - 500 rpm

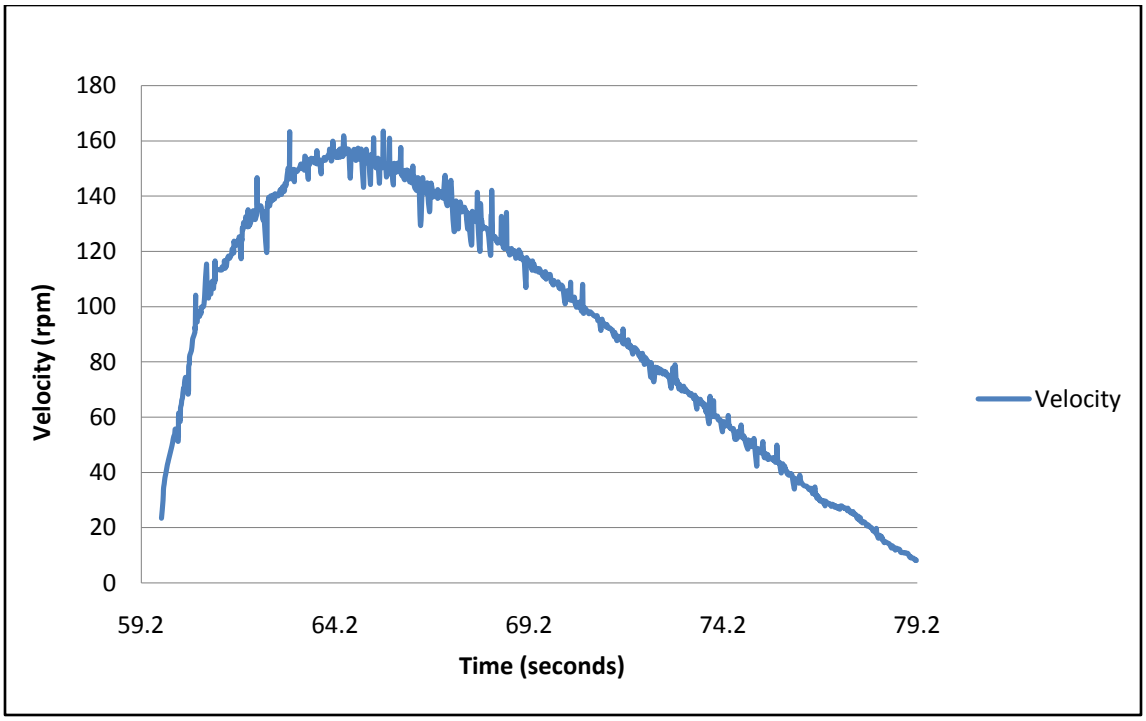

Figure 58: Output Flywheel Velocity Graph - 500 rpm

900 RPM Trial

The third set of trial data was collected using an input speed of 900 rpm and a clutch frequency of 5 Hz. Looking at the data obtained from the input encoder, a position plot, seen in Figure 59, was generated. Then, by taking the derivative of the position data, a velocity plot was created. In order to minimize the error in the data set, a moving average was applied. Figure 60 is a graph of the velocity with the applied moving average.

Using the same procedure, position and velocity graphs were obtained for the intermediate shaft and output flywheel. The intermediate position and velocity graphs are seen in Figure 61 and Figure 62, respectively. The output flywheel position and velocity graphs are seen in Figure 63 and Figure 64, respectively.

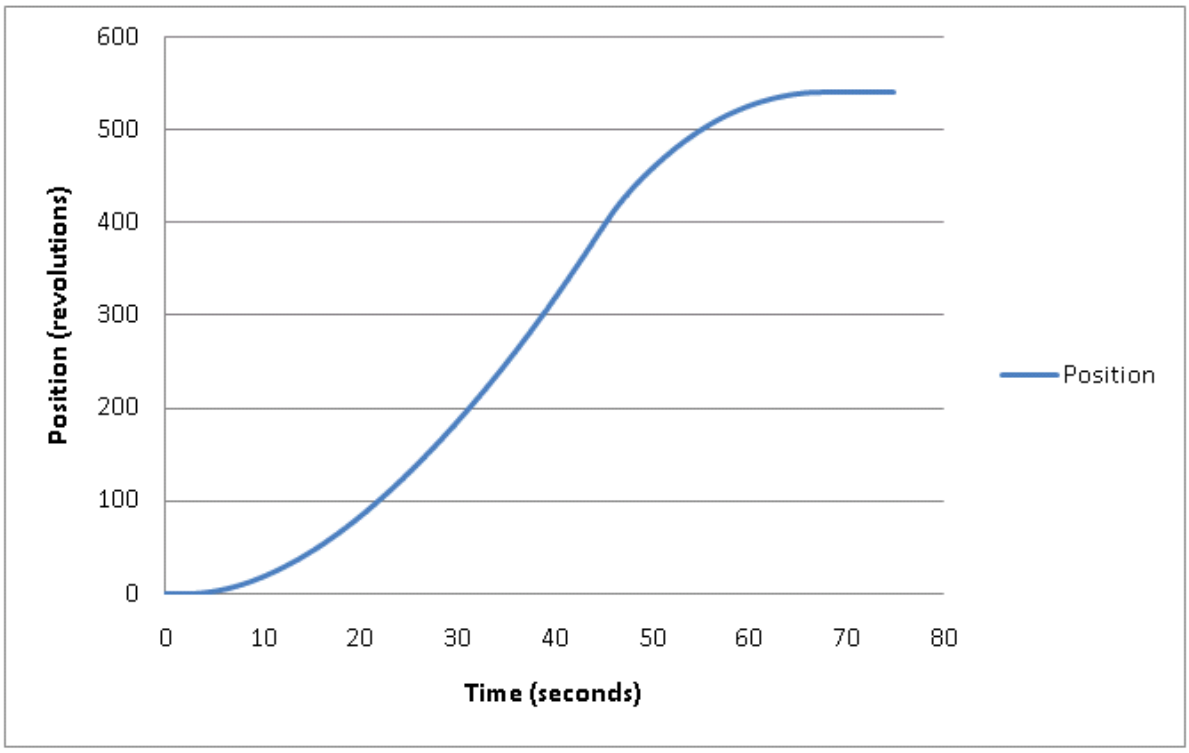

Figure 59: Input Flywheel Position Graph - 900 rpm

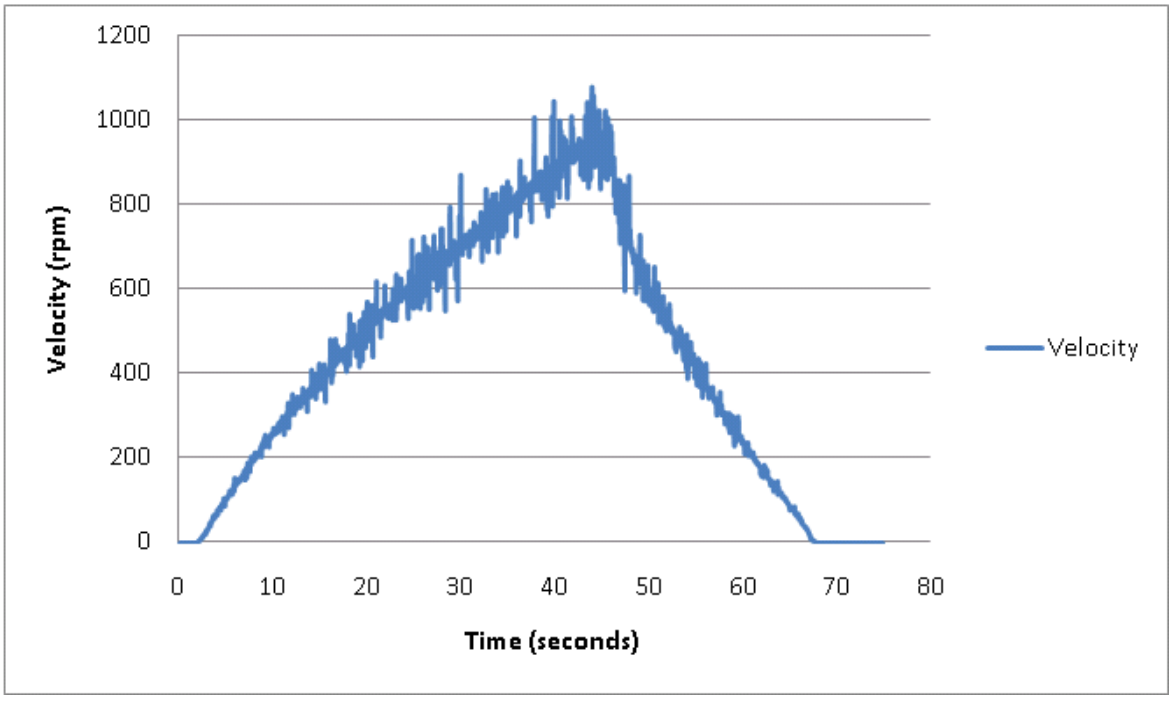

Figure 60: Input Flywheel Velocity Graph - 900 rpm

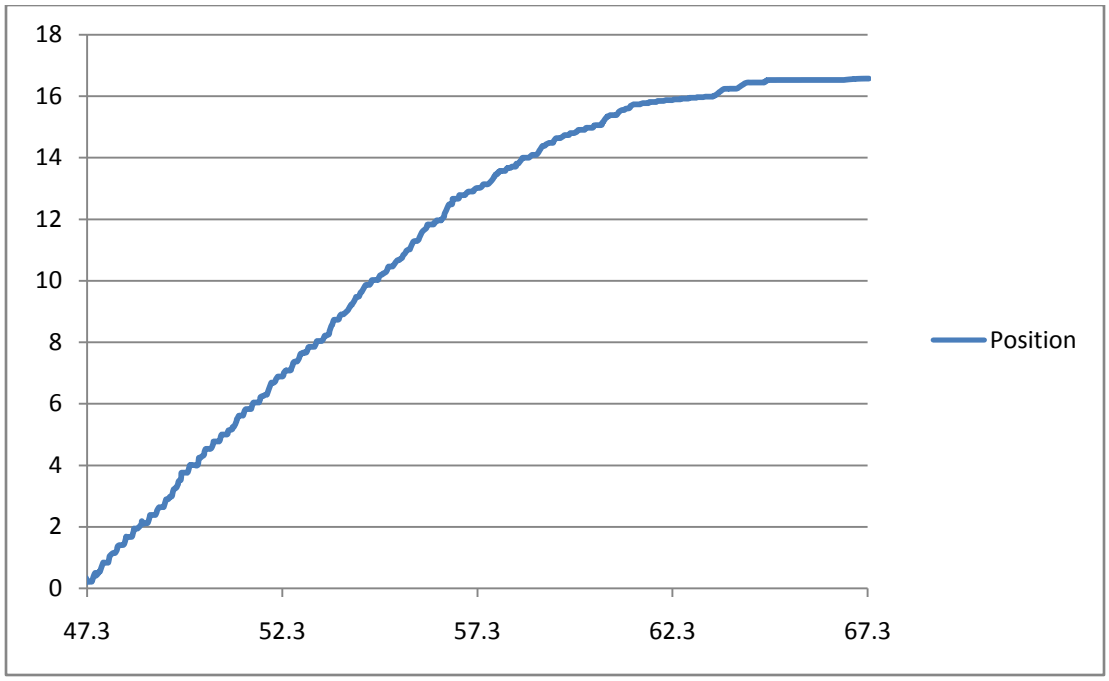

Figure 61: Intermediate Shaft Position Graph - 900 rpm

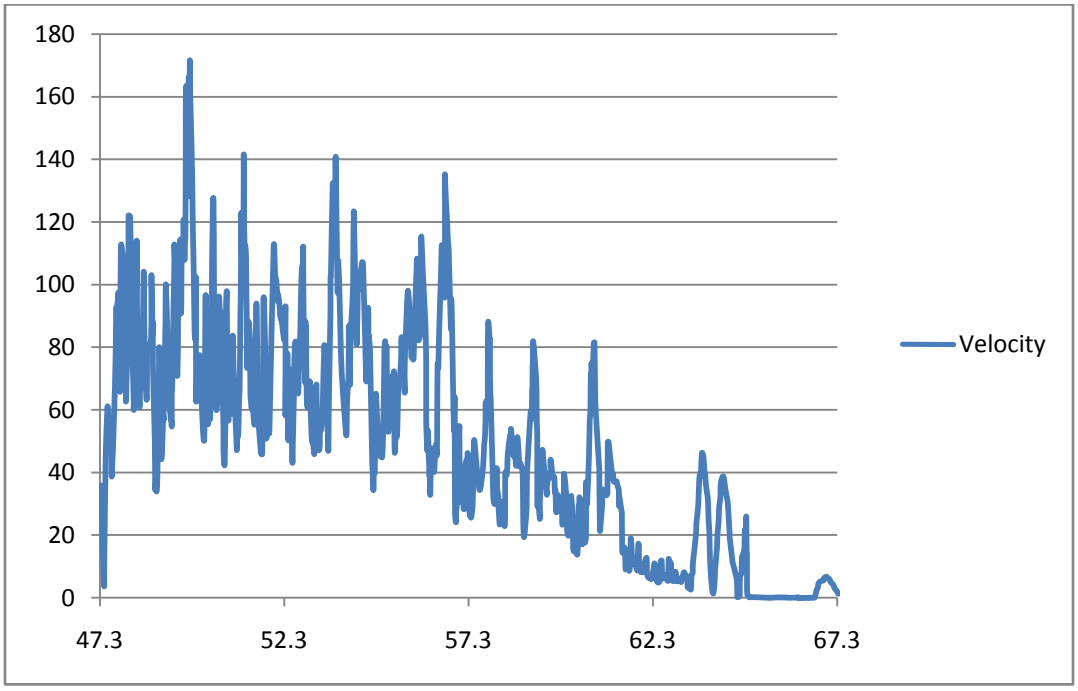

Figure 62: Intermediate Shaft Velocity Graph - 900 rpm

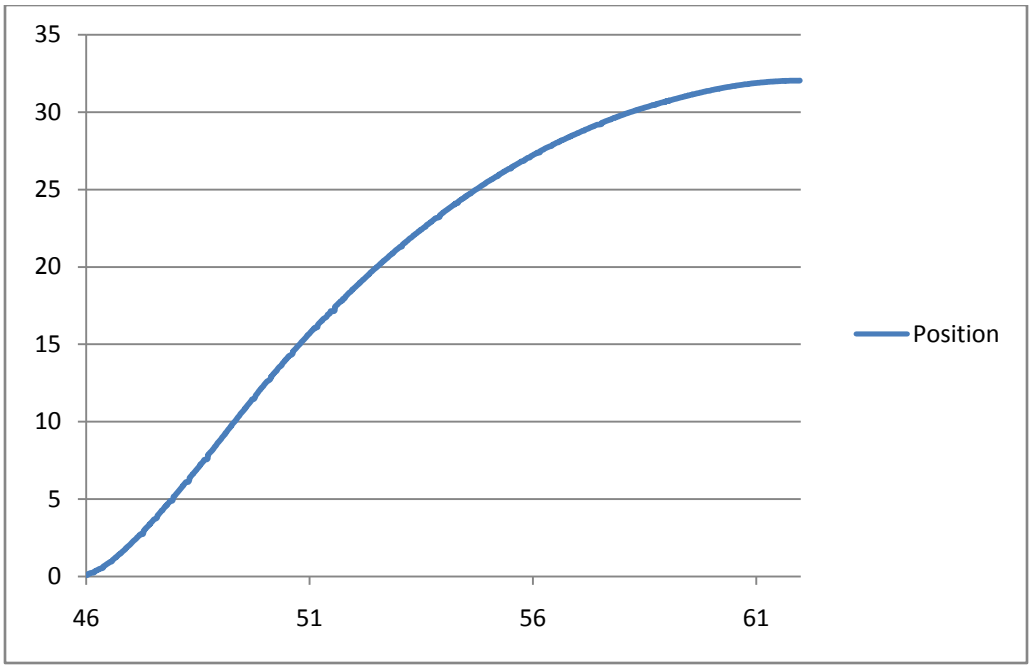

Figure 63: Output Flywheel Position Graph - 900 rpm

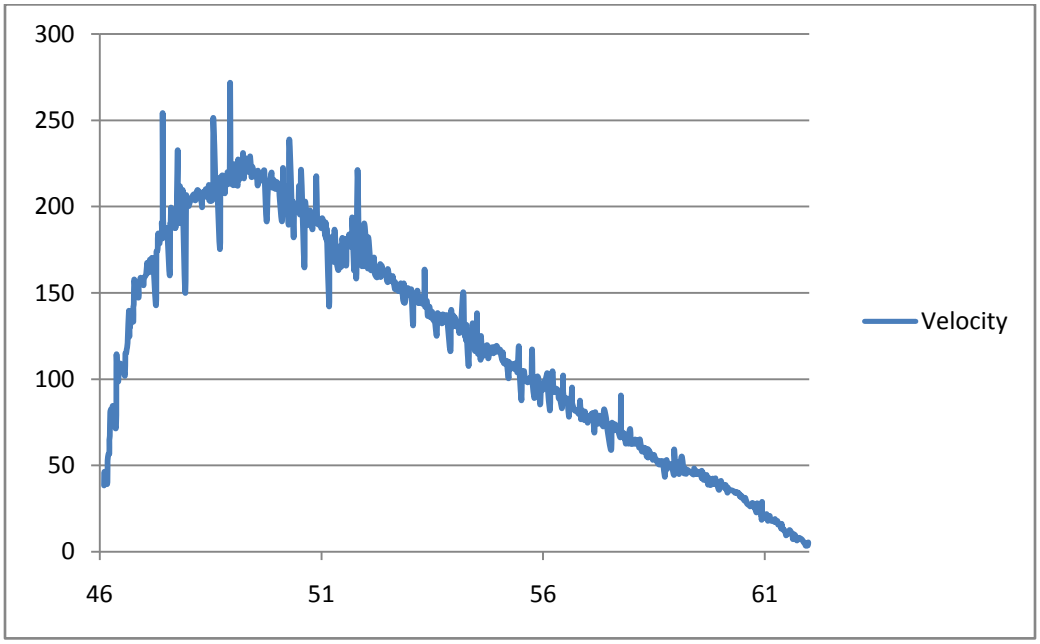

Figure 64: Output Flywheel Velocity Graph - 900 rpm

Discussion

This section of the paper is devoted to further explaining the results and any discrepancies or anomalies within the data. It is necessary to compare the experimental data with the hypothesized or predicted data from the MATLAB code. The main focal points were to examine the effects of the clutch and spring on the three portions of the system: input, intermediate, and output.

Spring Rate

When comparing the results of the spring rate test to the spring rate used in the MATLAB model, the values of which were 5.12 Nm/rad and 6.02 Nm/rad, respectively. The corresponding error was calculated at 17.54%. Some possible sources of error could be in the instrumentation used and conversion factors. The deflection was found using a protractor and an inexact mark on the flywheel. Also, the spring scale was held by hand and it was possible that the force measured was inaccurate. Finally, the force, deflection, and radius were measured in English units and needed to be converted to SI units to calculate the spring rate and make it comparable to the MATLAB model. Some of the inaccuracy can then also be attributed to rounding errors in the conversion factors.

Frictional Losses

The frictional losses in the system were examined on both the input and output flywheels. In order to create the equations, which were provided in the plots in the previous section, each flywheel needed to be spun to any speed and the decaying velocity tracked. The encoders were used to record the position of each flywheel and a position graph was created. Using an instantaneous velocity approach, an average derivate was taken over 10 terms of position data. This helped to minimize noise and showed the velocity trend for each flywheel. A quadratic trendline was fit to the resulting velocity graph. This equation had three terms, where the constant term was the peak velocity of the flywheel and the other two were the decay constants within the system. Some of the potential sources of loss in the flywheels include friction from the bearings inside the mounts, air, the encoders on the shaft, and the flanges connecting the components. Although some of these resistances may be negligible with respect to others, it was pertinent to mention where all possible losses could arise.

The equation showing the velocity decay of the input and output flywheels are as follows:

$$\omega_{input} = .0552t_0^2 - 12.249t_0 + \omega_0 \quad \textbf{(17)}$$

$$\omega_{output} = .0777t_0^2 - 8.7214t_0 + \omega_0 \quad \textbf{(18)}$$

where ω_{input} is the angular velocity of the input flywheel, ω_{output} is the angular velocity of the output flywheel, t_0 is time and ω_0 is the initial angular velocity.

Looking at the equations, it is clear that several things are contributing to the frictional losses within the system. The spinning flywheels are losing speed linearly due to coulomb friction within the bearings. They are also losing speed from aerodynamic drag. After spinning the flywheel to the desired speed and entering this parameter into the equation, the anticipated speed of the flywheel at a certain time can be approximated by entering that time value into the equation. The speed loss due to both friction and drag can then be quantified for a given trial run.

The experimental data, in the Results section, provided the proof of concept the project was searching to find. The following section looks to summarize the project by re evaluating the successes and failures of the project goals and to provide guidance for future projects and research on the topic.

Input

The input flywheel was predicted to experience an increase in velocity up to the desired speed due to input torque from the driving motor. Then, with each engagement of the clutch, an incremental decrease in input velocity would occur which correlated to the transfer of energy to the spring. There would also be a steady decline due to frictional decay within the system.

The experimental data, however, varied from the predicted results. The overall trend of the velocity was correct by showing the constant decay from friction and energy transfer, but the actual steps were not shown. A few potential reasons for the lack of these steps were attributed to the susceptibility of noise within the encoder, the uneven time step, and the method for calculating the velocity, which amplified the noise in the plot. In order to calculate velocity, an instantaneous approach was used. The approach took the change in position from one data point to the next and divided it by the change in time between the two data points. However, the

encoders recorded data at uneven time intervals, which was most likely brought about by voltage variation or an issue with the computers processor speed causing the CPU clock to be inaccurate.. The uneven time steps posed as a problem within the calculations because multiple data points were being collected at the same time. Although they added large spikes to the data the uneven time step was not entirely responsible for all the variation. The noise on the input side of the system created problems within the encoder as it showed jumps in the position value at inconsistent rates. Due to these inconsistencies, the instantaneous velocity showed erratic points but they were unable to be filtered because of the large quantity present. In the end, it was necessary to use a moving average for the instantaneous velocity to minimize the effect of noise within the graphs. However, once the moving average was applied to the data, any possibility for the pulse step appearing was eliminated due to the smoothing of the curve.

Intermediate

Looking at the intermediate shaft of the prototype, it was predicted that the shaft would produce incremental position changes due to the engagement of the clutch. The plot would create a staircase until all the energy from the flywheel was transferred through the system. Figure 65 is a graph of the position changes that occurred with two engagements of the clutch. As stated before, this model did not take into consideration the effects of damping on the intermediate shaft. With regards to the velocity, the model showed that for every engagement, the intermediate shaft experienced an increase in speed until it reached the input flywheel speed and then decreased to zero.

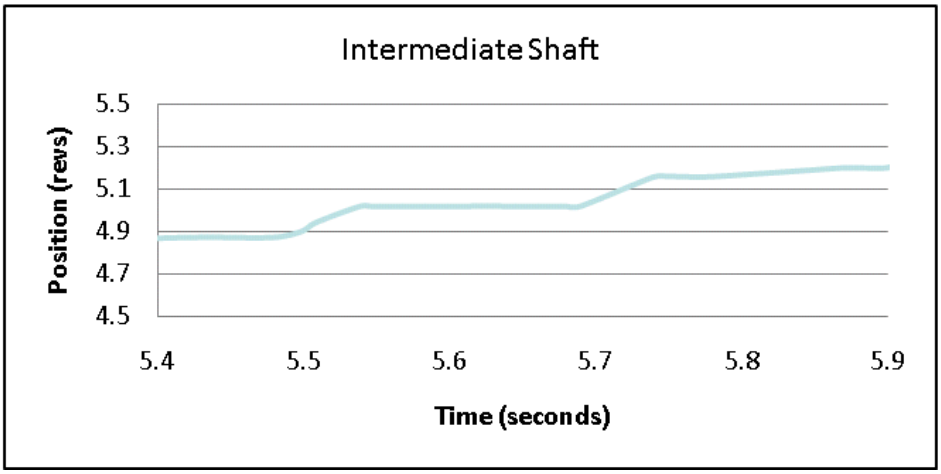

Figure 65: Intermediate Shaft Position

The experimental data showed small deviations from the model due to both the damping and vibrations in the system. Each position plot shown, in the previous section, exhibited the same characteristics as the predicted model. However, the damping in the system caused the shaft to slow down exponentially quickly rather than producing a linear descent.

The velocity plots had more problems due to the amplification of noise. The same noise amplification problem presented itself again within the intermediate shaft because of a non concentric shaft, producing vertical translation, and slipping between the sprag bearing and the shaft. A moving average was applied to the data to reduce noise spikes in the velocity curve but doing so created errors in calculating the maximum shaft speed with each engagement. The plots presented previously demonstrated that the predicted model was accurate, but due to noise reduction and some manufacturing issues, there were deviations within the expected values.

Output

The final section of the prototype was the output encoder which looked at the position and velocity of the output flywheel. The MATLAB model predicted the output flywheel to show a smooth increase in the position but have an exponential change for the velocity of the output flywheel increased. The velocity was also predicted to show the same trend, peak when all the energy was transferred from the input flywheel, and decrease due to the losses in the system.

The results from the experimental data concluded that some predicted ideas were incorrect. The position graphs of each trial were smooth and showed no signs of pulses from the clutch. Additionally, the velocity plots showed more of a logarithmic ascent to peak value followed by the predicted decay from losses in the system. As with each section of the system, noise created large deviations of the velocity and the moving average was applied to minimize those effects.

Conclusions and Recommendations

From the introduction, there were three goals set forth to be accomplished. The first goal was to research and develop system requirements and performance specifications for the drive train in a full sized passenger vehicle. This goal was achieved through the use of the MATLAB model and equations discussed in the Methodology section of the paper. The requirements were placed into the mathematical model, while the specifications were defined by equations to set the desired functionality of the passenger vehicle.

The next goal was to design and analyze a scaled down prototype that demonstrates the drive train. This was achieved through multiple MathCAD files presented throughout the Methodology, a MATLAB code for the prototype, and a CAD generated model of the system. The MathCAD files provided the stresses and forces present within the scaled system, which constrained the size of each component. From there, a CAD model was created for geometric design and visualization. Additionally, the MATLAB code used all aforementioned parameters to create a theoretical model of a single pulse of the system and how each component would react.

The final goal was to build and demonstrate a bench top prototype of the system in both its generative and regenerative mode. Within the Methodology, the prototype designed in the project was discussed to show the governing parameters around the modeling. After the manufacturing phase was completed, the system was constructed and data was collected. The data was presented in the Results chapter and discussed within the Discussion chapter. Overall, this goal was nearly completed; however, the system was only tested in the generative mode. Additionally, the system should be tested in its regenerative mode to prove the hypothetical model.

Although most of the goals were satisfied, there is still plenty of research and development left for future work. This project set the foundations for the potential of creating a full sized drive train; however, multiple areas are recommended for additional research and improvement. First, an appropriate clutch needs to be manufactured as no current model is able to handle the specifications of 20 Hertz and produce a sizeable amount of torque, much larger than the current 5 ft-lb. It is also recommended to improve the DAQ system in the prototype.

This could be as simple as finding more efficient encoders that are less susceptible to noise or use a wireless setup to track the position of the three shafts.

Secondly, the spring needs to be improved to both simplify the manufacturability of the system and create a better way to heat treat and cut the steel to an appropriate strength and size. The spring created for this prototype failed under a 1000 rpm load with many different factors contributing to its failure. When the spring bars were heat treated, they were clamped down between two pieces of steel without slots to place each bar. As a result, they came back slightly warped by the heat treatment. Recesses in the clamping pieces of steel could have kept the bars from expanding due to the heat treatment, and could have prevented warping. Another aspect of the failure of the bars was the duty ratio of the clutch at higher velocities. The duty ratio could have been set too high, which would have transferred more torque than the spring could safely handle under deflection. Decreasing the duty ratio at higher velocities would decrease the time the spring is under load and thus decrease the torque applied to the spring. Figure 66 is a picture of the failed spring under 1000 rpm load conditions.

Figure 66: Spring Failure

Overall, the project had a lot of success in achieving its goals. It was proved that the initial theoretical design is feasible but many areas need to be researched further before this design can be placed in a hybrid vehicle. This new technology has the potential to improve the efficiency of hybrid vehicles, help to eliminate the need for fossil fuels, and create higher emission standards for all vehicles.

References

Arora, J. S. (2004). Introduction to Optimum Design, Academic Press Page 426-427

Bejan, A. & Dincer, I. & Rosen, M. A. (2002). Thermal Energy Storage. Wiley Publishing Company Page 69-72

Bonsen, B. (2006). Efficiency optimization of the push-belt CVT by variator slip control. Retrieved September 16, 2008, from *www.em.tue.nl/pdfs/Bonsen%20Bram.pdf*

Continuously Variable Transmission. (2005). Ratcheting CVTs. Retrieved September 16, 2008, from http://cvt.com.sapo.pt/ratcheting/ratcheting.htm

Department of Transportation. (1998). Public Roads - January/February 1998. Retrieved September 16, 2008, from http://www.tfhrc.gov/pubrds/janpr/ednotes.htm

Digikey. (2009). Digi-Key Corporation. Retrieved April 25, 2009, from http://www.digikey.com/

Environmental Protection Agency. (2008). Urban Dynamometer Driving Schedule (UDDS). Retrieved September 25, 2008, from http://www.epa.gov/nvfel/testing/dynamometer.htm

Forbes, T. & Van de Ven, J. (2008). Switch-Mode Continuously Variable Transmission with Flywheel Energy Storage. Retrieved from, 2008 ASME International Mechanical Engineering Congress and Exposition

Girotto, Adriano. (2006). Adjustable Velocity Ratio Mechanical Transmission. European Patent 1688645A1

Green Car Congress. (2008). Torotrak Infinitely Variable Transmission Finds Business in Outdoor Power, Targets Hybrids for the Future. Retrieved September 16, 2008, from http://www.greencarcongress.com/2005/12/torotrak_infini.html

How Stuff Works. (2008). How CVTs Work. Retrieved September 16, 2008, from http://auto.howstuffworks.com/cvt2.htm

Huston, D.R. & Zhao, X. (2000). Whole-Body Shock and Vibration: Frequency and Amplitude Dependence of Comfort. Journal of Sound and Vibration (2000) 230(4), 964-970

Nakashima, A. (2004). The effect of vibration on human performance and health: A review of recent literature. Retrieved September 16, 2008, from http://pubs.drdc.gc.ca/PDFS/unc48/p523433.pdf

National Instruments. (2009). NI PC-6220 - Products and Services. Retrieved April 25, 2009, from http://sine.ni.com/nips/cds/view/p/lang/en/nid/14130

National Instruments. (2009). NI PCI-6601 - Products and Services. Retrieved April 25, 2009, from http://sine.ni.com/nips/cds/view/p/lang/en/nid/3589

Rasmussen, G. (2008). Human Body Vibration Exposure and Its Measurement. Retrieved October 5, 2008, from http://www.zainea.com/body.htm

Rondinelli, A. (2008). Warko – The CVT. Retrieved September 15, 2008, from http://www.warko.it/index.php?option=com_content&task=view&id=5&Itemid=8

SAE. (2008). Audi takes CVT from 15th century to 21st century. Retrieved September 16, 2008, from http://www.sae.org/automag/techbriefs_01-00/03.htm

SAE. (2009). Transmission Options. Retrieved September 16, 2008, from http://www.sae.org/automag/features/transopt/page5.htm

University of Minnesota. (2009). Motor/Switch/LED. Retrieved April 29, 2009, from http://www.me.umn.edu/education/courses/me2011/robot/technotes/motorswitchled/index.html

US Digital. (2009). Hollow Bore, Optical Encoder. Retrieved April 25, 2009, from http://usdigital.com/products/encoders/incremental/rotary/hollow-bore/hb6m/

Widmer, J. & von Burg, P. (1995). Failure of Tangentially Wound Composite Energy Storage Flywheels. Retrieved October 5, 2008, from http://www.aspes.ch/publications/EnerComp2.pdf

Yoshihiro Yoshida et al. (2005). Hydrostatic continuously variable transmission. US Patent 2005/0198953 A1.

Appendices

Appendix A: MATLAB Code

```
for i=2:timesteps  %Outside loop for each timestep

    if mod(i*delta_t, 1/freq) < timeon %Determining if clutch is on or off
        clutch(i) = 1; %Clutch on
    else
        clutch(i) = 0; %Clutch off
    end

    omega1(i) = sqrt(2*E1(i-1)/I1); %rad/s  Ang Vel of Flywheel 1
    omega3(i) = sqrt(2*E3(i-1)/I3); %rad/s  Ang Vel of Flywheel 3

    if clutch(i) == 1  %if clutch is on, ang vel of input of spring = ang vel of flywheel 1
        omega2(i) = omega1(i);
    else %clutch off
        if theta2(i-1) > theta3(i-1) % if there is deflection in the spring, ratchet holds input of spring
            omega2(i) = 0;
        else  %no deflcetion in spring, thus input of spring freewheels
            omega2(i) = omega3(i);
        end
    end

    %Setting ang position equal to previous ang position + omega*dt
    theta1(i) = theta1(i-1) + omega1(i)*delta_t;
    theta2(i) = theta2(i-1) + omega2(i)*delta_t;
    theta3(i) = theta3(i-1) + omega3(i)*delta_t;

    %Calculating spring torque due to spring rate and damping (functions of
    %dtheta and domega respectively)
    Ts(i) = k * (theta2(i) - theta3(i));
    Tb(i) = b * (omega2(i) - omega3(i));

    fr = fo + 3.24 * fs * (omega3(i)*dia/2/44.7)^2.5; %Calculating effective rolling resistance coeff
    Rx = fr * m * g; %N  Force due to rolling resistance
    Da = .5 * rho * A * Cd * (omega3(i)*dia/2)^2; %N  Force due to aero drag
    Td(i) = (Rx + Da) * dia/2; %Total drag torque (rolling drag + aero drag)*radius

    if mod(i*delta_t, 1/freq) < timeon  %if the clutch is on, apply torque of spring and damper
        E1(i) = .5 * I1 * omega1(i)^2 + omega1(i) * delta_t * (-Ts(i) - Tb(i)); %Energy in Flywheel 1
    else
        E1(i) = .5 * I1 * omega1(i)^2;  %if clutch is disengaged, energy is constant
    end
    E3(i) = .5 * I3 * omega3(i)^2 + omega3(i) * delta_t * (Ts(i) + Tb(i) - Td(i)); %Energy in Flywheel 3
    Es(i) = .5 * k * (theta2(i) - theta3(i))^2; %Energy in Spring

end  %end of for  --timesteps for model
```

Appendix B: Deflection Calculations

Constants α and β											
b/t	1.0	1.5	1.8	2.0	2.5	3.0	4	6	8	10	∞
α	0.208	0.231	0.239	0.246	0.258	0.267	0.282	0.299	0.307	0.313	0.333
β	0.141	0.198	0.214	0.299	0.249	0.263	0.281	0.299	0.307	0.313	0.333

$K := 684.466 \frac{N \cdot m}{rad}$ Spring constant given by COSMOS

$\theta := 113.494 deg$ Deflection given by COSMOS

$\%E_k := \left(\frac{K - K_t}{K}\right) \cdot 100 = 6.625$ Percent error of spring constant calculations

$\%E_x := \left|\left(\frac{\theta - \theta_v}{\theta}\right)\right| \cdot 100 = 7.095$ Percent error of deflection calculations

$E := 3.04579 \cdot 10^{7} \frac{lbf}{in^2}$ Youngs Modulus

$G := 11.5 \cdot 10^{6} \frac{lbf}{in^2}$ Shear Modulus

$b := .20in$ Bar thickness

$h := .60in$ Bar height

$r := 1in$ Radius from center

$L := 36in$ Lenght of bars

$\frac{h}{b} = 3$ Ratio of height to thickness

$\beta := .263$ Constant

$K_b := \frac{E \cdot h \cdot b^3}{4L^3} = 137.191 \cdot \frac{N}{m}$ Bending spring constant

$K_{to} := \frac{G \cdot \beta \cdot h \cdot b^3}{L} = 45.563 \cdot \frac{N \cdot m}{rad}$ Torsional spring constant

$K_{b2} := K_b \cdot r^2 = 0.089 \cdot \frac{N \cdot m}{rad}$ Bending spring constant

$Number := 14$ Number of bars

$K_t := Number \cdot (K_{b2} + K_{to}) = 639.121 \frac{N \cdot m}{rad}$ Total spring constant

$T_{max} := 1000lbf \cdot ft = 1.356 \times 10^3 \cdot N \cdot m$ Torque transfered

$\theta_v := \frac{T_{max}}{K_t} = 121.546 \cdot deg$ Total angular deflection

Appendix C: Clutch VI

Block Diagram

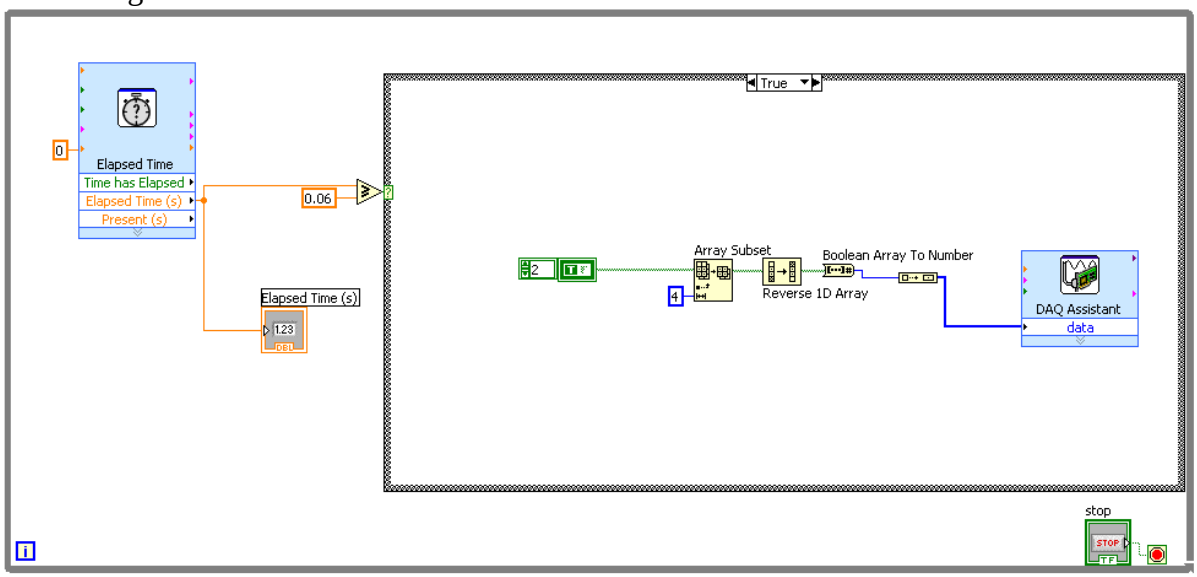

Front Panel

Appendix D: Encoder VI

Block Diagram

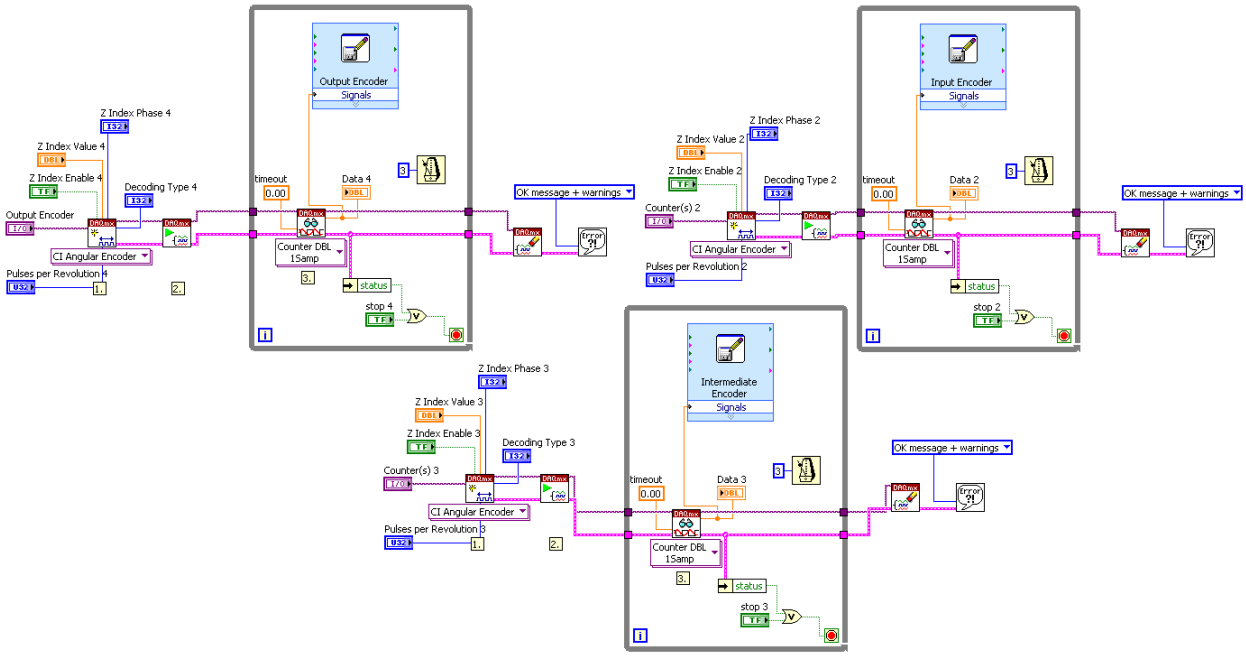

Front Panel